ADVCOMP 2023

The Seventeenth International Conference on Advanced Engineering Computing and Applications in Sciences

ISBN: 978-1-68558-107-7

September 25 - 29, 2023

Porto, Portugal

ADVCOMP 2023 Editors

Alice Koniges, University of Hawaii, USA

José Miguel Jimenez, Universitat Politecnica de Valencia, Spain

ADVCOMP 2023

Forward

The Seventeenth International Conference on Advanced Engineering Computing and Applications in Sciences (ADVCOMP 2023), held between September 25th and September 29th, 2023, continued a series of international events meant to bring together researchers from the academia and practitioners from the industry in order to address fundamentals of advanced scientific computing and specific mechanisms and algorithms for particular sciences.

With the advent of high-performance computing environments, virtualization, distributed and parallel computing, as well as the increasing memory, storage and computational power, processing particularly complex scientific applications and voluminous data is more affordable. With the current computing software, hardware and distributed platforms, effective use of advanced computing techniques is more achievable.

The conference provided a forum where researchers were able to present recent research results and new research problems and directions related to them. The conference sought contributions presenting novel research in all aspects of new scientific methods for computing and hybrid methods for computing optimization, as well as advanced algorithms and computational procedures, software and hardware solutions dealing with specific domains of science.

We take here the opportunity to warmly thank all the members of the ADVCOMP 2023 technical program committee, as well as all the reviewers. The creation of such a high-quality conference program would not have been possible without their involvement. We also kindly thank all the authors who dedicated much of their time and effort to contribute to ADVCOMP 2023. We truly believe that, thanks to all these efforts, the final conference program consisted of top-quality contributions. We also thank the members of the ADVCOMP 2023 organizing committee for their help in handling the logistics of this event.

We hope that ADVCOMP 2023 was a successful international forum for the exchange of ideas and results between academia and industry and for the promotion of progress related to advanced engineering computing and applications in sciences.

ADVCOMP 2023 Chairs

ADVCOMP 2023 Steering Committee
Dean Vucinic, Vrije Universiteit Brussel (VUB), Belgium, FERIT, Croatia
Juha Röning, University of Oulu, Finland
Hans-Joachim Bungartz, TUM, Germany
Marcin Hojny, AGH University of Science and Technology, Poland
Andreas Rausch, TU Clausthal, Clausthal-Zellerfeld, Germany
Alice E. Koniges, University of Hawai'i at Mānoa, USA

ADVCOMP 2023 Publicity Chairs
Laura Garcia, Universitat Politecnica de Valencia, Spain
Lorena Parra Boronat, Universitat Politecnica de Valencia, Spain

ADVCOMP 2023
Committee

ADVCOMP 2023 Steering Committee

Dean Vucinic, Vrije Universiteit Brussel (VUB), Belgium, FERIT, Croatia
Juha Röning, University of Oulu, Finland
Hans-Joachim Bungartz, TUM, Germany
Marcin Hojny, AGH University of Science and Technology, Poland
Andreas Rausch, TU Clausthal, Clausthal-Zellerfeld, Germany
Alice E. Koniges, University of Hawai'i at Mānoa, USA

ADVCOMP 2023 Publicity Chairs

Laura Garcia, Universitat Politecnica de Valencia, Spain
Lorena Parra Boronat, Universitat Politecnica de Valencia, Spain

ADVCOMP 2023 Technical Program Committee

Waleed H. Abdulla, University of Auckland, New Zealand
José Abellán, Catholic University of Murcia, Spain
Mohamed Riduan Abid, Alakhawayn University, Morocco
Rashmi Agrawal, Manav Rachna International Institute of Research and Studies, India
Francisco Airton Silva, Federal University of Piauí, Brazil
M. Azeem Akbar, Nanjing University of Aeronautics and Astronautics, China
Haifa Alharthi, Saudi Electronic University, Saudi Arabia
Sónia Maria Almeida da Luz, Polytechnic Institute of Leiria - School of Technology and Management, Portugal
Madyan Alsenwi, Kyung Hee University, Global Campus, South Korea
Mohamed E. Aly, California State Polytechnic University, Pomona, USA
Daniel Andresen, Kansas State University, USA
Anindya Das Antar, University of Michigan, USA
Alberto Antonietti, Politecnico di Milano / University of Pavia, Italy
Mansur Arief, Carnegie Mellon University, Pittsburgh, USA
Abhinav Arora, Meta Platforms, USA
Ehsan Atoofian, Lakehead University, Canada
Vadim Azhmyakov, Universidad Central, Bogota, Republic of Colombia
Carlos Becker Westphall, University of Santa Catarina, Brazil
Raoudha Ben Djemaa, ISITCOM | University of Sousse, Tunisia
Peter Bentley, University College London, UK
Sergiy Bogomolov, Newcastle University, UK
Alessandro Borri, CNR-IASI Biomathematics Laboratory, Rome, Italy
David Bouck-Standen, Kingsbridge Research Center, UK
Sofiane Bououden, University Abbes Laghrour Khenchela, Algeria
Hans-Joachim Bungartz, TUM, Germany
Xiao-Chuan Cai, University of Colorado Boulder, USA
Jadson Castro Gertrudes, Federal University of Ouro Preto, Brazil

Graziana Cavone, Polytechnic of Bari, Italy
Mete Celik, Erciyes University, Turkey
Jieyang Chen, Oak Ridge National Laboratory, USA
Jinyuan Chen, Louisiana Tech University, USA
Vassilios V. Dimakopoulos, University of Ioannina, Greece
Inês Domingues, IPO Porto Research Centre (CI-IPOP), Portugal
Maha Elarbi, University of Tunis, Tunisia
Javier Fabra, Universidad de Zaragoza, Spain
Akemi Galvez, University of Cantabria, Spain / Toho University, Japan
Tong Geng, Boston University, USA
Jing Gong, KTH Royal Institute of Technology, Sweden
Teofilo Gonzalez, UC Santa Barbara, USA
Maki Habib, American University in Cairo, Egypt
Yang He, University of Technology Sydney, Australia
Mohd Helmy Abd Wahab, Universiti Tun Hussein Onn Malaysia, Malaysia
Marcin Hojny, AGH University of Science and Technology, Poland
Wladyslaw Homenda, Warsaw University of Technology, Poland
Tzung-Pei Hong, National University of Kaohsiung, Taiwan
Mehdi Hosseinzadeh, Washington University in St. Louis, USA
Paul Humphreys, Ulster University | Ulster University Business School, UK
Andres Iglesias, University of Cantabria, Spain / Toho University, Japan
Joanna Isabelle Olszewska, University of West Scotland, UK
Hiroshi Ishikawa, Tokyo Metropolitan University, Japan
Félix J. García Clemente, University of Murcia, Spain
Rishabh Joshi, Google Research - Brain Team, USA
Attila Kertesz, University of Szeged, Hungary
Zaheer Khan, University of the West of England, UK
Alice E. Koniges, University of Hawai‘i at Mānoa, USA
Seyong Lee, Oak Ridge National Laboratory, USA
Maurizio Leotta, University of Genova, Italy
Clement Leung, Chinese University of Hong Kong, Shenzhen, China
Yiu-Wing Leung, Hong Kong Baptist University, Hong Kong
Yiheng Liang, Bridgewater State University, USA
Stephane Maag, Telecom SudParis, France
Elbert E. N. Macau, Federal University of Sao Paulo - UNIFESP at Sao Jose dos Campos, Brazil
Rafael Magdalena Benedicto, University of Valencia, Spain
Marcin Markowski, Wroclaw University of Science and Technology, Poland
Mirko Marras, University of Cagliari, Italy
Yoan Martinez Lopez, Camagüey University, Cuba
René Meier, Hochschule Luzern, Switzerland
Mohamed Wiem Mkaouer, Rochester Institute of Technology, USA
Sébastien Monnet, Savoie Mont Blanc University (USMB), France
Shana Moothedath, University of Washington, Seattle, USA
Laurent Nana, University of Brest, France
Ehsan Nekouei, City University of Hong Kong, Hong Kong
Kaiming Ouyang, Nvidia, USA
Marcin Paprzycki, Systems Research Institute | Polish Academy of Sciences, Poland
Prantosh Kumar Paul, Raiganj University, India

Damien Pellier, Université Grenoble Alpes, France
Sonia Pérez-Díaz, University of Alcalá, Spain
Antonio Petitti, Institute of Intelligent Industrial Systems and Technologies for Advanced Manufacturing (STIIMA) - National Research Council of Italy (CNR) , Italy
Tamas Pflanzner, University of Szeged, Hungary
Agostino Poggi, Università degli Studi di Parma, Italy
Evgeny Pyshkin, University of Aizu, Japan
Andreas Rausch, Technische Universität Clausthal, Germany
Michele Roccotelli, Politecnico di Bari, Italy
Ivan Rodero, Rutgers University, USA
Juha Röning, University of Oulu, Finland
Diego P. Ruiz, University of Granada, Spain
Bibhudatta Sahoo, National Institute of Technology, Rourkela, India
Julio Sahuquillo, Universitat Politècnica de València, Spain
Subhash Saini, NASA, USA
Aadesh Salecha, University of Minnesota, USA
Shailaja Sampat, Arizona State University, USA
Hamed Sarvari, George Mason University, USA
Alireza Shahrabi, Glasgow Caledonian University, Scotland, UK
Justin Shi, Temple University, USA
Piotr Sowiński, Systems Research Institute, Polish Academy of Sciences, Poland
Sudarshan Srinivasan, Oak Ridge National Laboratory, USA
Mohammed Tanash, Kansas State University, USA
Yeming Tang, Pennsylvania State University, USA
Costas Vassilakis, University of the Peloponnese, Greece
Bhavan Vasu, Oregon State University, USA
Flavien Vernier, LISTIC – Savoie University, France
Juan Vicente Capella Hernández, Universitat Politècnica de València, Spain
Dean Vucinic, Vrije Universiteit Brussel (VUB), Belgium / FERIT, Croatia
Guangjing Wang, Michigan State University, USA
Hanrui Wang, Massachusetts Institute of Technology, USA
Lei Wang, University of Connecticut, USA
Shi Wenxuan, Nankai University, China
Adriano V. Werhli, Universidade Federal do Rio Grande - FURG, Brazil
Gabriel Wittum, Goethe University Frankfurt, Germany
Zongshen Wu, University of Wisconsin, Madison, USA
Mudasser F. Wyne, National University, USA
Cong-Cong Xing, Nicholls State University, USA
Feng Yan, University of Nevada, Reno, USA
Limin Yang, University of Illinois at Urbana-Champaign, USA
Carolina Yukari Veludo Watanabe, Federal Unversity of Rondônia, Brazil
Michael Zapf, Technische Hochschule Nürnberg Georg Simon Ohm (University of Applied Sciences Nuremberg), Germany
Vesna Zeljkovic, Lincoln University, USA
Ruochen Zeng, NXP Semiconductors, USA
Penghui Zhang, Arizona State University, USA
Qian Zhang, Liverpool John Moores University, UK

Copyright Information

For your reference, this is the text governing the copyright release for material published by IARIA.

The copyright release is a transfer of publication rights, which allows IARIA and its partners to drive the dissemination of the published material. This allows IARIA to give articles increased visibility via distribution, inclusion in libraries, and arrangements for submission to indexes.

I, the undersigned, declare that the article is original, and that I represent the authors of this article in the copyright release matters. If this work has been done as work-for-hire, I have obtained all necessary clearances to execute a copyright release. I hereby irrevocably transfer exclusive copyright for this material to IARIA. I give IARIA permission or reproduce the work in any media format such as, but not limited to, print, digital, or electronic. I give IARIA permission to distribute the materials without restriction to any institutions or individuals. I give IARIA permission to submit the work for inclusion in article repositories as IARIA sees fit.

I, the undersigned, declare that to the best of my knowledge, the article is does not contain libelous or otherwise unlawful contents or invading the right of privacy or infringing on a proprietary right.

Following the copyright release, any circulated version of the article must bear the copyright notice and any header and footer information that IARIA applies to the published article.

IARIA grants royalty-free permission to the authors to disseminate the work, under the above provisions, for any academic, commercial, or industrial use. IARIA grants royalty-free permission to any individuals or institutions to make the article available electronically, online, or in print.

IARIA acknowledges that rights to any algorithm, process, procedure, apparatus, or articles of manufacture remain with the authors and their employers.

I, the undersigned, understand that IARIA will not be liable, in contract, tort (including, without limitation, negligence), pre-contract or other representations (other than fraudulent misrepresentations) or otherwise in connection with the publication of my work.

Exception to the above is made for work-for-hire performed while employed by the government. In that case, copyright to the material remains with the said government. The rightful owners (authors and government entity) grant unlimited and unrestricted permission to IARIA, IARIA's contractors, and IARIA's partners to further distribute the work.

Table of Contents

Optimized Hardware Configuration for High Performance Computing Systems 1
Scott Hutchison, Daniel Andresen, William Hsu, Mitchell Neilsen, and Benjamin Parsons

Multifractal Analysis of Thermal Images of Electronic Devices in Different Colour Profiles 7
Marina Diaz-Jimenez, Juan Carlos de la Torre, Javier Jareno-Dorado, Patricia Ruiz, Bernabe Dorronsoro, and Pablo Pavon-Dominguez

A Graphical Analysis of the Multimodal Public Transport Network – The Bay of Cadiz 14
Patricia Camacho Magrinan, Pablo Pavon Dominguez, and Patricia Ruiz

A Survey of Recent Applications of the PISALE Code and PDE Framework 20
Alice Koniges, David Eder, Jonghyun Lee, Aaron Fisher, Yuriy Mileyko, Monique Chyba, Jack McKee, Young-Ho Seo, Peter Yip, Thomas Schwartzentruber, Claudia Parisuana, and Siegfried Glenzer

Optimized Hardware Configuration for High Performance Computing Systems

Scott Hutchison
Department of Computer Science
Kansas State University
Manhattan, KS 66505, USA
email: scotthutch@ksu.edu

Daniel Andresen
Department of Computer Science
Kansas State University
Manhattan, KS 66505, USA
email: dan@ksu.edu

William Hsu
Department of Computer Science
Kansas State University
Manhattan, KS 66505, USA
email: bhsu@ksu.edu

Mitchell Neilsen
Department of Computer Science
Kansas State University
Manhattan, KS 66505, USA
email: neilsen@ksu.edu

Benjamin Parsons
High Performance Computing Modernization Program
Engineering Research and Development Center
Vicksburg, MS 39180, USA
email: ben.s.parsons@erdc.dren.mil

***Abstract*—When faced with upgrading or replacing High Performance Computing or High Throughput Computing systems, system administrators can be overwhelmed by hardware options. Servers come with various configurations of memory, processors, and hardware accelerators, like graphics cards. Differing server capabilities greatly affect their performance and their resulting cost. For a fixed budget, it is often difficult to determine what server package composition will maximize the performance of these systems once they are purchased and installed. This research uses simulation to evaluate the performance of different server packages on a set of jobs, and then trains a machine learning model to predict the performance of un-simulated server package compositions. In addition to being orders of magnitude faster than conducting simulations, this model is used to power a recommender system that provides a precision@50 of 92%.**

***Index Terms*—HPC; Procurement Optimization; Recommender system; XGBoost.**

I. Introduction

When faced with upgrading or expanding a High Performance Computing (HPC) or High Throughput Computing (HTC) system, administrators of these systems can be overwhelmed by options. It is a challenging task to get the best performance for a fixed budget. Server capabilities (i.e., number and types of processors, amount of memory, and number and types of Graphics Processing Units (GPU) or other hardware accelerators) greatly affect their costs, and for a fixed spending ceiling, it is desirable to get the "best bang for your buck." For an HPC system, an optimal server package composition is dictated by its typical use. For instance, if many users rely upon a GPU-accelerated application or library, a higher GPU count may be desirable, even if this means fewer servers can be purchased. With many factors to consider, HPC administrators often rely upon their preferences, intuition, and experience to inform procurement decisions. This research uses historical job data from an HPC system, a discrete event simulator, and a machine learning model to power a recommender system, which can help inform a hardware procurement decision. These techniques provide additional information to HPC system administrators about which set of budget-constrained hardware minimizes wait time for users' jobs, and provides quantifiable support for procurement decisions when upgrading or expanding existing HPC infrastructure. The contributions of this work can be summarized as follows:

1) A data set consisting of roughly 12,700 HPC scheduling simulations, each with a different HPC server set
2) An optimized XGBoost regression model for predicting average wait time when given a composition of servers
3) A recommender system with precision@50=92%, which can inform hardware procurement decisions

This paper is laid out as follows: Section II provides additional background on the problem and describes similar work done by others, Section III provides the methodology and some implementation details, Section IV provides details of formulas for metric calculations, Section V provides the results of the experiments, and Sections VI provides our final conclusions.

II. Background and Related Works

The Open Science Grid (OSG) [1] [2] is a worldwide collaboration that offers distributed computing for scientific research. In the central United States, one of the organizations contributing resources to the OSG is the Great Plains Augmented Regional Gateway to the Open Science Grid (GP-ARGO) [3]. In part, GP-ARGO receives funding through governmental grants. These grants are often used to procure new equipment to expand or improve the capabilities of GP-ARGO's participating organizations. Consequentially, there is a fixed budget ceiling for HPC equipment procurement, and the administrator's goal is to purchase new equipment that will maximize computational performance for our typical applications while ensuring costs remain under the fixed grant budget. The research question for this work is as follows: for a

Copyright (c) IARIA, 2023. ISBN: 978-1-68558-107-7

planned HPC expansion, can experimental simulation provide an optimal set of hardware under a given budget that will minimize job wait time?

The challenge of optimal hardware procurement is not exclusive to our organization. Similar work was done by Evans et al. [4]. They collected benchmarks for various software applications on different hardware to optimize the ratio of Central Processing Unit (CPU) and GPU architectures for HPC jobs. Their work is similar to ours, but we took a different approach by using a scheduling simulator to evaluate the performance of a set of jobs that were actually submitted to an HPC system. We are solving a very similar problem as Evans et al., but using a different approach to arrive at an optimal hardware configuration.

Other researchers have attempted to optimize for a particular application, such as the work Kutzner et al. [5] did to improve the utilization of GPU nodes when using GROMACs. Although these techniques are not without their merits for HPC systems that run a large number of homogeneous applications, users of the GP-ARGO HPC systems run a wide variety of jobs and applications. A more broad scheduler-based optimization was more appropriate for our application.

Various public HPC workloads exist [6], and have been used by HPC researchers in the past. However, as we are attempting to identify and evaluate new hardware for a specific HPC system, log data from that HPC system was utilized as the workload for this research.

Different scheduling applications like SLURM, HTCondor, or PBS, operate on HPC systems and perform the function of assigning HPC resources to jobs. This job to machine assignment task is as an extension of the online bin packing problem [7]. For the bin packing problem, the goal is to pack a sequence of items with sizes between 0 and 1 into as few bins of size 1 as possible. Each job specifies the resources requested (the object sizes), and each HPC machine has a certain amount of available resources (the bins with their respective sizes). The scheduler is given the task to meet job requirements by assigning them to HPC nodes (pack the objects into the available bins) as efficiently as possible. This is an online problem as new jobs are submitted over time to the scheduler. The best fit bin packing (BFBP) algorithm has been shown by Dosa and Sgall [8] to use at most $\lfloor 1.7OPT \rfloor$ bins, ensuring this algorithm will provide a reasonably close to optimal average wait time when it is used as an HPC job scheduling algorithm. Since scheduling algorithms vary between applications, most being highly customizable, and others being proprietary, a discrete event simulator utilizing the BFBP algorithm served as a stand-in for our scheduling application in an attempt to make it more universally applicable. The BFBP scheduling algorithm is described in Figure 1.

Although various HPC simulators have been used for similar research, such as SimGrid [9], GridSim [10], or Alea [11], this experiment needed a simple discrete event simulator using the BFBP scheduler. The simulators mentioned above were either deemed overly complex for our purposes, or they failed to allow for the three limiting resources (memory, CPUs, and GPUs) we were interested in investigating. An HPC scheduler simulator was also considered, such as the SLURM simulator developed at SUNY University in Buffalo [12]. Although this option was investigated further, scaling a job's actual duration from the log data to the new machine once it is assigned to a machine was challenging. As such, a custom discrete event simulator was developed and utilized for this research. The simulator allows for three resource constraints in each machine: memory, CPUs, and GPUs. It is fairly lightweight, fast, and easy to understand.

Algorithm 1 Best Fit Bin Packing Scheduling

```
1: while The simulation is incomplete do
2:     if Some job in the queue can be executed on some machine then
3:         Find the (job, machine) pairing which results in the fewest remaining resources for some machine. Begin executing that job on that machine.
4:     else
5:         Advance simulation time until a new job is submitted or a running job ends, whichever is sooner.
6:         Queue submitted jobs and stop ending jobs.
7:     end if
8: end while
```

Fig. 1. Pseudocode for the best fit bin packing algorithm

A significant consideration when evaluating new server hardware is the performance increase newer technology or architectures can provide. Using log data, we know how long a job took on a machine with known hardware. Since the specifications for the new hardware under consideration are also known, the actual duration of the jobs from the historic log data was scaled using base performance of the processor as reported by SPEC CPU2017 benchmark, second quarter, 2023 [13].

Knowing how a particular job performed on one set of hardware and estimating how it will perform on some other hypothetical set of hardware is challenging. Sharkawi et al. [14] successfully used a similar SPEC benchmark to estimate the performance projections of HPC applications. Other researchers, like Wang et al. [15] have pointed out that these benchmarks fail to account for all the variables affecting job resource utilization and should be avoided. Although CPU performance is not the only factor by which we could have scaled job duration, and perhaps it is not the best factor by which to scale, it worked well for our purposes. The discrete event simulator was implemented such that the scaling factor could be easily changed if other researchers should find a different factor more relevant to their situation.

Various metrics are typically used when evaluating the performance of HPC scheduling algorithms. Some of these are average wait time, HPC utilization, average turnaround time, makespan, throughput, etc. Which metric is used depends on

Copyright (c) IARIA, 2023. ISBN: 978-1-68558-107-7

the application and function of the HPC system, and different organizations may value one metric over another. The metric used for this research was average wait time, or the average number of seconds each job spent waiting in the job queue for execution on HPC resources. We presume that the same techniques could be applied by other researchers using a different metric, should they prefer a different one.

Recommender systems power a variety of applications like search engines and music recommendation systems. First, the hits for the system must be defined. Hits are the elements from the data set that are relevant to the user's search. Next, the user specifies the number of recommendations, k, that they would like to receive. If the recommender system is precise, a large portion of the k items returned will be hits.

III. Methodology

The general plan for optimizing a hardware package for our fixed budget can be summarized as follows:

1) Receive vendor quotes with potential server options.
2) Generate potential server combinations to purchase under the specified budget which meet our procurement requirements.
3) Identify a typical set of jobs representing the workloads typically submitted to our HPC system.
4) Conduct simulations using a subset of the server packages to schedule the representative job set and compute metrics to determine their performances.
5) Use machine learning to train and refine a model that can predict the performance of un-simulated server combinations.
6) Develop a recommender system using the machine learning model.
7) Subjectively evaluate the recommended server packages and make a more informed procurement decision.

A. Generate Server Options

To begin, we received several vendor quotes specifying the costs and capabilities of 21 potential servers to purchase. When considering upgrade options, we typically separate servers into one of three categories: compute nodes, big memory nodes, or GPU nodes. A compute node typically has a large number of processor cores, a moderate amount of memory, and no GPU. A big memory node will have a large amount of memory with a moderate amount of CPU cores and no GPU. A GPU node is any node which has a GPU. Table I lays out the options we received from several different vendors. The procurement budget was fixed at $1 million, and all possible server combinations were generated in the following way:

- Separate servers into three categories: compute nodes, big memory nodes, and GPU nodes.
- Choose all combinations of one node from each category.
- Determine all quantities of the three node types under a given budget such that there is at least one GPU node and there is not enough funding remaining to purchase another node.

TABLE I. Server capabilities and costs under investigation

Node type	*Distinct nodes considered*	*Memory range per node*	*CPUs range per node*	*GPUs per node*	*Cost range per node*
Compute	4	256-512 Gb	24-64 cores	0 GPUs	$6k-$10k
Big memory	2	1024 Gb	24-64 cores	0 GPUs	$11k-$13k
GPU	15	256-1024 Gb	24-64 cores	1-8 GPUs	$14k-$100k

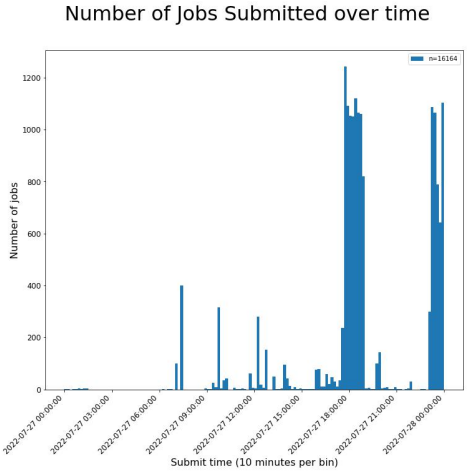

Fig. 2. The number of jobs submitted over time for the selected day

In our selected job set, many jobs requested GPUs as a resource. These jobs would automatically fail if at least one GPU node were not included in a potential server package. Roughly 127,000 different server combinations met these requirements. Table II provides an illustrative example of how the server combinations were generated. Many server options and packages were omitted from the table for the sake of brevity.

B. Identify a Representative Set of Jobs

One typical day's worth of submitted jobs (roughly 16,000 jobs) was subjectively pulled from the log data of the local HPC system. As with most HPC systems, jobs were submitted in a bursty manner, and variety of resources were requested. Figure 2 and Table III display some descriptive statistics and information about the jobs used by this research.

C. Job Duration Scaling

The submitted jobs were scaled using the base performance of the processor on the SPEC CPU2017 benchmark suite. The requested duration was not modified, but the actual duration of each job was calculated using the following formula:

$$\text{New duration} = \frac{\text{logged duration} * \text{logged processor performance}}{\text{new processor performance}}$$

D. Discrete Event Simulator

A discrete event simulator was implemented in Python that provides the following functionality:

Copyright (c) IARIA, 2023. ISBN: 978-1-68558-107-7

TABLE II. GENERATED SERVER COMBINATIONS

ComputeNode1, $6,960 ea.	*BigMemNode1, $11,112 ea.*	*GPUNode1, $14,730 ea.*	...	*Package Cost*	*Funds Remaining*
141	0	1	...	$996,090	$3,910
139	1	1	...	$993,282	$6,718
138	2	1	...	$997,434	$2,566
⋮	⋮	⋮	⋱	⋮	⋮
0	1	67	...	$998,022	$1,978

TABLE III. DESCRIPTIVE STATISTICS FOR THE POOL OF SELECTED JOBS

	Requested Mem (in Gb)	*Requested CPUs*	*Requested GPUs*	*Requested Duration (in hours)*	*Actual Duration (in hours)*
Mean	5.12	4.75	0.002	2.82	2.27
Std Dev.	16.73	3.33	0.055	1.02	13.67
Min	1	1	0	0	0
Max	800	64	4	11.20	11.20

- A global clock to keep track of simulation time.
- Several queues, priority queues, or lists to track jobs as they progress through the execution process: future jobs, queued jobs, running jobs, completed jobs, and unrunnable jobs.
- Jobs and machines are specified using comma separated value (csv) files, which is loaded prior to the simulation.
- Machines have three limiting resources: available memory, CPUs, and GPUs.
- Jobs are specified with the following attributes: submit time, actual duration, and requested duration, memory, CPUs, and GPUs. Jobs track their start time and end time as the simulation progresses to allow for metric calculation.
- Job end time is set when the job starts running as the job start time plus the job actual duration.
- When a job starts running on a machine, that machine's available resources are decremented by the resources requested by the job. Conversely, when a job completes, the machine executing it has its available resources increased by the amount requested by the ending job.
- Jobs with a submit time greater than the current global clock reside in the future jobs priority queue.
- Jobs with a submit time less than or equal to the current global clock, but not yet assigned to a machine, reside in the job queue.
- Jobs that have begun their execution and have an ending time less than the current global clock, reside in the running jobs priority queue.
- Jobs with an ending time less than or equal to the current global clock reside in the completed jobs list.
- If no node in the cluster has adequate resources to run a particular job, that job is moved to the unrunnable jobs list.
- In the event that no queued jobs can run on available resources, the simulation time "fast forwards" to the next event: either job submission or job ending.
- Jobs in the job queue are run as soon as there are available resources and are chosen using the best fit bin packing scheduling algorithm described in Algorithm 1.
- Actual job duration from logged job data can be scaled to allow for hardware improvement with newer hardware.

E. Machine Learning

Although each simulation completed fairly quickly, requiring no more than 30 minutes each, this particular combination of server quotes yielded roughly 127,000 combinations that need to be evaluated. To reduce the computational requirement, every tenth line from the file with the server combinations was sampled, and roughly 12,700 simulations for these server packages were completed in parallel using HPC resources. By sampling from the generated server packages uniformly, various quantities of each server under consideration were included in the simulated data. Each server package was summarized into the package total memory, total CPUs, and total GPUs, by summing the resources of every machine comprising the package. The average wait time for the simulation served as the label for each package. The data was split into 90% training and 10% test data, and an XGBoost [16] regression model was trained using training data. The regression model was evaluated using Root Mean Squared Error (RMSE) on the test data. An accurate regression model enabled the prediction of the average wait time for unsimulated server combinations and saved countless hours of additional simulation.

F. Recommender System

In our case, a hit was defined as a server combination with an average wait time in the lowest 5% of simulated combinations (or 632 hits out of the $\sim$12,700 simulated server combinations). The value of k was varied to evaluate the performance of the recommender system. Then, once confidence was gained that our recommender system was functioning properly, it was used to recommend systems from the entire server combination pool of 127,000 server combinations. The recommendations were summarized and evaluated subjectively before arriving at a final procurement decision.

G. Simplifying Assumptions

The current nodes comprising the HPC system were not added to the set of nodes simulating the selected jobs. The benefit current nodes would provide to the new servers under investigation would be common to all.

Any additional equipment required to install and operate the new servers (e.g., networking hardware, additional cooling equipment, server racks, power infrastructure, etc.) were not

Copyright (c) IARIA, 2023. ISBN: 978-1-68558-107-7

deducted from the total procurement budget. It was thought that these costs would be a relatively fixed regardless of the server package chosen. The same analysis described in this research could be done by reducing the total budget by the cost of additional hardware and then completing the analysis with a reduced budget.

IV. Evaluation

Pearson's Correlation Coefficient [17] determined the extent of the correlation between the total memory, CPUs, and GPUs of a package and the average wait time. This coefficient provides a value between -1 and 1, where values closer to -1 or 1 indicate that the feature and the label are more strongly correlated. A coefficient of 0 indicates no correlation.

Wait time was calculated by analyzing the completed jobs output from each simulation. The wait time for each job was the number of seconds from the time the job was submitted until it began. For N jobs, the average wait time was calculated as follows:

$$\text{AvgWaitTime} = \frac{\Sigma_{i=0}^{N}(\text{Start Time}_i - \text{Submit Time}_i)}{N}$$

Root Mean Squared Error was utilized for regression model evaluation calculated according to the following formula:

$$\text{RMSE} = \sqrt{\frac{\Sigma_{i=0}^{N}(\text{actual wait time}_i - \text{predicted wait time}_i)^2}{N}}$$

The performance of the final recommender system was evaluated using precision@k, recall@k, and F1@k. In general, precision@k is the proportion of recommended items in the top-k set that are relevant, and recall@k is the proportion of relevant items found in the top-k recommendations. F1@k is the harmonic mean of precision@k and recall@k, which simplifies them into a single metric. They were calculated according to the following formulas:

$$\text{Precision@k} = \frac{(\text{\# of recommended items @k that are relevant})}{(\text{\# of recommended items @k})}$$

$$\text{Recall@k} = \frac{(\text{\# of recommended items @k that are relevant})}{(\text{total \# of relevant items})}$$

$$\text{F1@k} = \frac{(2 * \text{precision@k} * \text{recall@k})}{(\text{precision@k} + \text{recall@k})}$$

V. Results

The correlation of features, the performance of the regression model and the recommender system, and some analysis about the recommended server compositions are described below.

A. Feature Correlation

The correlation between the features and the labels is shown in Table IV. For this set of jobs, the total CPUs in a server package were most strongly correlated to the average wait time. For the chosen jobs, the more CPUs a package had, the lower its average wait time.

Since we are constrained by our available budget of $1 million, choosing to buy one type of node over another is a zero-sum game. The more GPU nodes we purchase, and the more GPUs there are per node, the fewer compute nodes or big memory nodes we are able to afford. This is indicated by the positive correlation between GPUs and the average wait time.

TABLE IV. Pearson Correlation Coefficients

	TotalMem	*TotalCPUs*	*TotalGPUs*	*AvgWaitTime*
TotalMem	1.00	0.14	-0.54	-0.23
TotalCPUs	0.14	1.00	-0.42	-0.70
TotalGPUs	-0.54	-0.42	1.00	0.44
AvgWaitTime	-0.23	-0.70	0.44	1.00

B. Regression Model

The XGBoost regression model had a RMSE = 150.13 seconds, indicating that the total memory, CPUs, and GPU features made excellent predictors for the average wait time for these jobs when simulated with the discrete event simulator. The predicted vs. actual wait time is shown in Figure 3. If the regression model were perfect, all these points would lie upon the $y = x$ line, and it is clear that this model does a good job at predicting the average wait time for a given composition of servers.

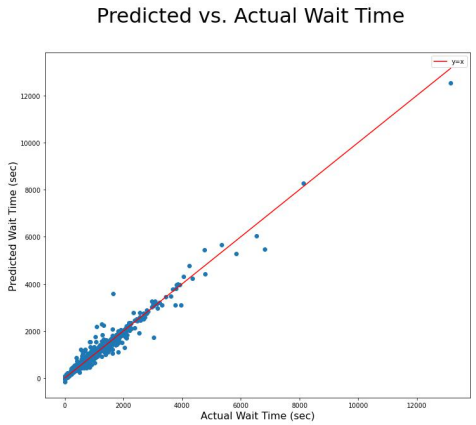

Fig. 3. The predicted vs. actual wait times showing the accuracy of our regression model.

C. Recommender System

The regression model was used to predict the 12,700 labeled simulations, and their precision@k, recall@k, and F1@k for various values of k are displayed in Table V. The goal was to reduce the number of possibilities from roughly 127,000 different possible combinations of servers down to a reasonable number which could be evaluated by an HPC system administrator and have a large percentage of the recommended server combinations be hits (among the best 5% of server combinations with the lowest average wait times). Although precision@10 was 100%, it is thought that seeing more server package options would allow system administrators a wider variety from which to choose. A system administrator could easily and quickly review up to 50 recommendations ($k = 50$), and more than 46 out of 50 of these recommendations returned

Copyright (c) IARIA, 2023. ISBN: 978-1-68558-107-7

by this system (92%) would be top performing server combinations, which is excellent. Recall@k when k is less than the number of total hits (632 hits total) is unfairly penalized, but the recall@k above 632 is also excellent. When $k = 1,000$, the recall@1000 = 91%, meaning the recommender system successfully retrieved 91% of the top 5% performing server packages when returning less than 1% of the 127,000 different options.

TABLE V. PRECISION@K AND RECALL@K FOR TEST DATA

k value	*Precision@k*	*Recall@k*	*F1@k*
10	1.00	0.02	0.03
50	0.92	0.07	0.13
100	0.81	0.13	0.22
500	0.74	0.59	0.66
632	0.72	0.72	0.72
1000	0.58	0.91	0.71

D. Recommended Compositions

Beyond looking at the individual server compositions recommended, we wanted to draw some conclusion about the types and quantity of nodes that the recommender system returned. The sum of the server quantities for the top 50 recommendations can be found in Table VI. Compute nodes with the larger number of cores were vastly preferred, and the recommender system did not recommend spending additional funds on more memory for the compute nodes. Additionally, the recommender system preferred the cheaper big memory node with fewer cores. Finally, for our typical workload, the recommender system did not recommended purchasing a large number of GPUs per GPU node, instead recommending servers with 2 GPUs per server most often. In terms of our budget breakdown, the recommender system suggests spending on average 58% of our total budget on compute nodes, 8% on big memory nodes, and 34% on GPU nodes.

TABLE VI. RECOMMENDATIONS DRAWN FROM MODEL PREDICTED RESULTS

Node Type	*Node Description*	*Sum of Servers Across Top 50*
Compute Nodes	Cheapest w/ 256Gb	232
	Cheapest w/ 512Gb	0
	Expensive w/ 256Gb	3,467
	Expensive w/ 512Gb	0
Big Memory Nodes	Cheapest w/ 1024Gb	232
	Expensive w/ 1024Gb	111
GPU Nodes	2 GPUs in one server	732
	4 GPUs in one server	267

VI. CONCLUSIONS

This recommender system is not intended to replace the expertise of HPC administrators when it comes to decisions for hardware procurement. It is our hope that this tool can provide a data-driven technique which will help narrow the search space with which administrators are confronted when they make procurement decisions. Returning to the research question: experimental simulation coupled with a regression model enabled a recommender system to return server compositions under a given budget with low average wait times with a precision@50 of 92%. Additionally, the discrete event simulator, job data set, machine learning code, and recommender system code are released under the GPLv3 license should other researchers find it useful [18].

REFERENCES

[1] R. Pordes *et al.*, "The open science grid," in *J. Phys. Conf. Ser.*, vol. 78 of *78*, p. 012057, 2007.

[2] I. Sfiligoi *et al.*, "The pilot way to grid resources using glideinwms," in *2009 WRI World Congress on Computer Science and Information Engineering*, vol. 2 of *2*, pp. 428–432, 2009.

[3] "The great plains augmented regional gateway to the open science grid." https://gp-argo.greatplains.net/. Accessed 2023-01-18.

[4] R. T. Evans *et al.*, "Optimizing gpu-enhanced hpc system and cloud procurements for scientific workloads," in *International Conference on High Performance Computing*, pp. 313–331, Springer, 2021.

[5] C. Kutzner *et al.*, "More bang for your buck: Improved use of gpu nodes for gromacs 2018," *Journal of computational chemistry*, vol. 40, no. 27, pp. 2418–2431, 2019.

[6] D. G. Feitelson, D. Tsafrir, and D. Krakov, "Experience with using the parallel workloads archive," *Journal of Parallel and Distributed Computing*, vol. 74, no. 10, pp. 2967–2982, 2014.

[7] S. Martello and P. Toth, *Knapsack problems: algorithms and computer implementations*. John Wiley & Sons, Inc., 1990.

[8] G. Dósa and J. Sgall, "Optimal analysis of best fit bin packing," in *Automata, Languages, and Programming: 41st International Colloquium, ICALP 2014, Copenhagen, Denmark, July 8-11, 2014, Proceedings, Part I 41*, pp. 429–441, Springer, 2014.

[9] H. Casanova, A. Giersch, A. Legrand, M. Quinson, and F. Suter, "Versatile, scalable, and accurate simulation of distributed applications and platforms," *Journal of Parallel and Distributed Computing*, vol. 74, pp. 2899–2917, June 2014.

[10] R. Buyya and M. Murshed, "Gridsim: A toolkit for the modeling and simulation of distributed resource management and scheduling for grid computing," *Concurrency and computation: practice and experience*, vol. 14, no. 13-15, pp. 1175–1220, 2002.

[11] D. Klusáček, M. Soysal, and F. Suter, "Alea–complex job scheduling simulator," in *Parallel Processing and Applied Mathematics: 13th International Conference, PPAM 2019, Bialystok, Poland, September 8–11, 2019, Revised Selected Papers, Part II 13*, pp. 217–229, Springer, 2020.

[12] N. A. Simakov *et al.*, "Slurm simulator: Improving slurm scheduler performance on large hpc systems by utilization of multiple controllers and node sharing," in *Proceedings of the Practice and Experience on Advanced Research Computing*, pp. 1–8, 2018.

[13] "Second quarter 2023 spec cpu2017 results," 2023. https://www.spec.org/cpu2017/results/res2023q2, Accessed on June 14, 2023.

[14] S. Sharkawi *et al.*, "Performance projection of hpc applications using spec cfp2006 benchmarks," in *2009 IEEE International Symposium on Parallel & Distributed Processing*, pp. 1–12, IEEE, 2009.

[15] Y. Wang, V. Lee, G.-Y. Wei, and D. Brooks, "Predicting new workload or cpu performance by analyzing public datasets," *ACM Transactions on Architecture and Code Optimization (TACO)*, vol. 15, no. 4, pp. 1–21, 2019.

[16] T. Chen and C. Guestrin, "Xgboost: A scalable tree boosting system," in *Proceedings of the 22nd ACM sigkdd international conference on knowledge discovery and data mining*, pp. 785–794, 2016.

[17] K. Pearson, "Note on regression and inheritance in the case of two parents," *Proceedings of the royal society of London*, vol. 58, no. 347-352, pp. 240–242, 1895.

[18] S. Hutchison, "Optimal-hardware-procurement-for-a-hpc-expansion." https://github.com/shutchison/Optimal-Hardware-Procurement-for-a-HPC-Expansion, Accessed on September 19, 2023.

Copyright (c) IARIA, 2023. ISBN: 978-1-68558-107-7

Multifractal Analysis of Thermal Images of Electronic Devices in Different Colour Profiles

Marina Díaz-Jiménez
Dept. Computer Science Eng.
University of Cádiz, Spain
email: marina.diaz@uca.es

Juan Carlos de la Torre
Dept. Computer Science Eng.
University of Cádiz, Spain
email: juan.detorre@uca.es

Javier Jareño-Dorado
Dept. Computer Science Eng.
University of Cádiz, Spain
email: javier.jareno@uca.es

Patricia Ruiz
Dept. Mechanical Eng. and Ind. Design
University of Cádiz, Spain
University of Sydney, Australia
email: patricia.ruiz@uca.es

Bernabé Dorronsoro
Dept. Computer Science Eng.
University of Cádiz, Spain
University of Sydney, Australia
email: bernabe.dorronsoro@uca.es

Pablo Pavón-Domínguez
Dept. Mechanical Eng. and Ind. Design
University of Cádiz, Spain
email: pablo.pavon@uca.es

***Abstract*—Nowadays, there are many methods for analysing images. Among them, a multifractal approach is able to characterise images in terms of the complexity of patterns they contain. However, multifractal methods are very sensitive to small changes in colour images. This study presents a preliminary study for the accurate characterisation of electronic devices in terms of heat dissipation using multifractal analysis. Specifically, a novel methodology using multifractal approach is proposed to characterise images in different colour formats: Grey-Scale, Red-Green-Blue (RGB), Cyan-Magenta-Yellow-Key (CMYK), Hue-Saturation-Value (HSV) and Hue-Saturation-Intensity (HSI), and the results are compared. For this purpose, thermal images of a Pi3 Raspbian Desktop board are analysed with the aim of finding out the results of the multifractal analysis on different areas of the board. Multifractal analysis is carried out through the box-counting method and the method of moments, since they allow to extract the main multifractal parameters, such as, the generalised dimensions function, $D(q)$ and the degree of multifractality, $\Delta D(q)$. The results obtained show that both scaling properties and multifractal parameters vary according to the colour format, i.e., the same image exhibits different multifractal properties depending on the colour format.**

Keywords - Multifractal analysis; thermal images; colour formats; box-counting; colour images.

I. Introduction

Fractal shapes are mainly characterised by self-similar properties and a fractal dimension (D_f), which is dependent of the scaling measure [1]. However, in some structures, due to geometrical complexity, several fractal structures overlap simultaneously and are considered as multifractal objects [2]. These multifractal objects are completely characterised by a function, known as a generalised dimensions function ($D(q)$) [3]. The box-counting method and the method of moments [4] allow to carry out a simple and robust multifractal analysis on images. These methods are able to estimate the generalised fractal dimensions, $D(q)$, and describe complex structures with sets of regions exhibiting different fractal properties, providing a relatively more concrete characterisation.

From a fractal approach, image analysis is typically accomplished on binary [5] or RGB images [6] [7]; however, they are hardly found from a multifractal approach nor in different colour formats [8] [9]. For this reason, a novel methodology for analysing images in different colour formats by means of multifractal analysis is proposed in this work. Specifically, four well-known formats namely RGB, CMYK, HSV and HSI, are analysed and compared using the multifractal box-counting method. The analysis has been carried out on thermal images of a Pi3 Raspbian Desktop board, in order to make a first approach towards the characterisation of electronic devices based on heat dissipation. Additionally, three different areas of the board are analysed, in order to provide our study with different cases of study. Results show that the multifractal analysis varies depending on the colour profile, i.e., the same image, depending on the colour format, presents different multifractal properties. This result points out that the image colour profile may hinder the multifractal properties of the heat dissipation of the electronic device. Therefore, it is concluded that in order to carry out a multifractal analysis of thermal images, the raw file should ideally be considered to avoid alterations in the results.

The paper is organised as follows. Section II briefly presents the most relevant works in the state of the art. Section III introduces the methodology proposed in this work. Thermal image acquisition and multifractal analysis are described in sections III-A and III-B, respectively. Results are explained in Section IV. Finally, Section V concludes the work.

II. Related Works

Fractal analysis has extensively been used for the analysis of digital images [5], however, there are few studies of digital colour images using a more comprehensive approach, the multifractal analysis. Most of the existing fractal methods for analysing images are defined for 1D signal or binary images, extending to Grey-Scale images [5]. In [8], a multifractal analysis using the box-counting method is applied on RGB images. Specifically, the authors analyse a three-dimensional histogram of the image, which contains the R, G and B colour coordinates. In the same way, in [10] the three-dimensional

Copyright (c) IARIA, 2023. ISBN: 978-1-68558-107-7

histogram of RGB images is also analysed. However, here, the authors use the multifractal analysis as an image noise detection tool. In works such as [9], RGB images are analysed by decomposing the channels that make up each image. They propose a methodology similar to the one proposed in this work. However, they only select one channel from the RGB image and then binarise it, so the multifractal analysis is actually conducted on binary images, unlike the proposed work, where the pixels of the analysed images take values from 0 to 255. Furthermore, in this work, not only are RGB images analysed, but also images in different colour formats (including all the channels that compose each format). Moreover, [6] highlights the difficulty in estimating the fractal dimension of RGB colour images. Finally, [7] again analyses RGB and Grey-Scale images from a fractal approach using the box-counting method. The authors adopt a methodology similar to the one followed in this work, since they analyse a Grey-Scale image as well as each of the channels that make up the RGB image.

As it can be seen, the number of existing studies on images considering different colour formats from a multifractal approach is low. For this reason, the purpose of this work is to present a new methodology, using multifractal analysis, to characterise images in different colour formats, in order to evaluate the influence of the colour format in the results of the analysis. Specifically, this work is focused on analysing thermal images of an electronic device with the aim of establishing robust relationships between the multifractal characteristics of the device and heat dissipation in the future.

III. Methodology

This section is structured in two subsections. Section III-A summarises the thermal images under study, as well as the image capture process and image processing. Then, the multifractal analysis approach and its application to the study of thermal images is explained in Section III-B.

A. Thermal images

The images under study correspond to a Pi3 Raspbian Desktop board, on which the basal consumption was evaluated. That is, the images are captured during the base consumption of the Operating System, from an initial state, when the board is turned off, to a second state, after one hour, when the board is on. It should be noted that the images were taken by the authors. The images in the different colour profiles have also been created by them.

The image capture is performed by a FLIR ETS320 infrared camera, which allows the visualisation of hot spots and potential failure points, capturing the emissivity of the object. This camera model has a wide temperature range $[-20°\text{C}, 250°]$ with a measurement accuracy of $\pm 3°\text{C}$, allowing to quantify the heat generation and heat dissipation of small components (up to 170 μm). It consist of an InfraRed (IR) Sensor, which offers 76,800 points of non-contact temperature measurement. Finally, standard radiometric jpeg files are obtained, with 14 bit measurement data.

Image capture is carried out for one hour (3,600 seconds), from an initial time ($t_0 = 0s$) when the board is off, to a second time ($t_1 = 3,600s$), so the board is on for an hour. During this time period, a total of 31,970 images of the board were captured, at an average of 8-9 images per second. This camera model produces rectangular images of 320x240 pixels. In Figure 1, an example of the captured images is shown.

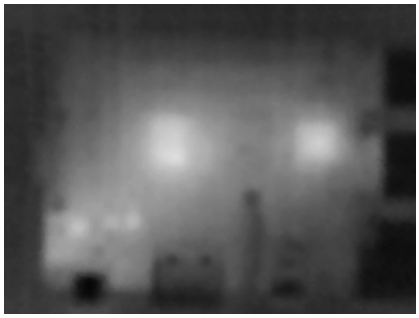

Figure 1. Example of a 320x240 pixel image of the board.

The subsequent method used for multifractal analysis requires that the analysed images must be square with a side length power of 2. For this, each of the rectangular images on the board is cropped into different square sub-images of 128x128 pixels. Specifically, this study focuses on three different areas of the board at three different time instants. In this way, three 128x128 pixels square cutouts were obtained, each one corresponding to a different time instant, which are independent of each other (see Figure 2). It should be noted that each of the images in Figure 2 will be studied, from a multifractal approach, in different colour profiles: Grey-Scale (GS), RGB, CMYK, HSV and HSI (see Figure 3).

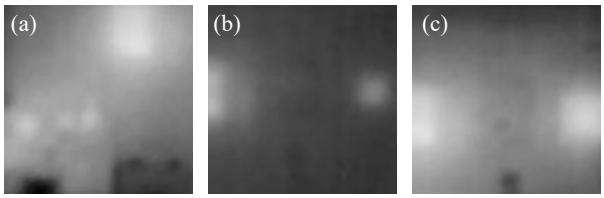

Figure 2. Images of different areas of the board at different time instants, (a) Image area 1, (b) Image area 2, (c) Image area 3.

As already mentioned, the images obtained by the infrared camera represent the emissivity values captured by the IR sensor (values from 0.0 to 1.0). Subsequently, a normalisation is carried out, where these values between 0 and 1 become the values of a Grey-Scale image (values between 0 and 255). These Grey-Scale images are used as a reference, because they are considered to represent the most faithful and realistic situation to the raw files captured by the camera.

B. Multifractal Analysis

Fractal shapes are mainly characterised by the fact that the measurement of the object is dependent on the scale of measurement. When this dependence follows a power law, it

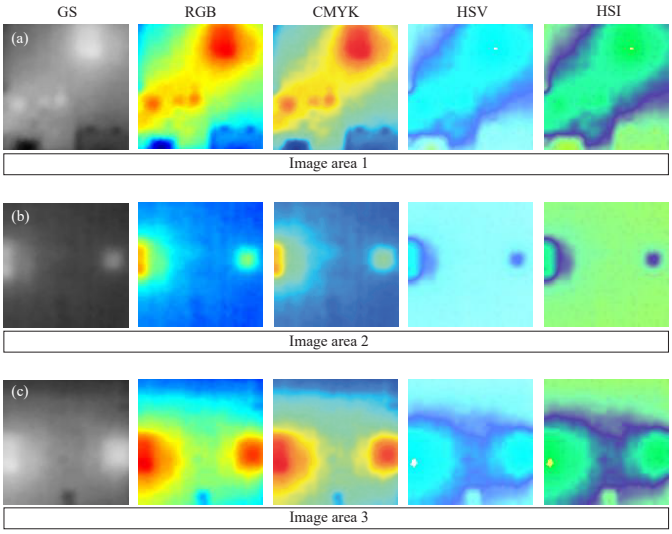

Figure 3. Images corresponding to the three defined areas of the board in each of the four different colour profiles: RGB, CMYK, HSK, HSI, and the Grey-Scale image (GS).

is said that the object manifests fractal properties. The main parameter is known as the fractal dimension (D_f), which is estimated by means of the slope of the linear fit on the log-log relationship between the scale and the measure [11] [12]. However, due to geometrical complexity, several fractal structures overlap simultaneously and are considered as multifractal objects. Multifractal objects are completely characterised by a function, known as a generalised dimensions function, $D(q)$ [13] [14]. The main advantage of multifractal analysis is the description of complex structures exhibiting sets of regions with different fractal properties, providing a relatively more specific characterisation [2].

To carry out the multifractal analysis, it is proposed to use the box-counting method along with the method of moments [4]. These methods allow a robust estimation of the generalised fractal dimensions, $D(q)$ [13] [14]. In the box-counting method, an image of side L is completely covered by a set of square boxes, of side δ, which do not overlap. Values of δ are obtained as follows: $\delta = \{L/1, L/2, L/4, L/8, ...\}$. Regarding the method of moments, parameter q is a remarkable one, which is a real value varying between $-\infty$ and $+\infty$ [2]. Positive q values magnify regions with high colour intensity values, while negative q values intensify regions with low colour intensity values. With these methods, the partition function, $\chi(q,\delta) = \sum_{i=1}^{n}(c_i(\delta))^q$, is obtained, being $(c_i(\delta))^q$ the mass probability function. It is well known that multifractality appears when the existence of a power law between $\chi(q,\delta)$ vs. δ is trusted. This function allows to differentiate the scale ranges (δ) where the linear fits will be performed. In this work, it is taken as a criterion to select the scale range where all the moments q can be considered, both positive and negative, and where, in addition, there is linearity. Once the range of scales is established, we turn to the generalised dimensions function, $D(q) = \frac{\tau(q)}{q-1}$, where $\tau(q)$ is the mass exponent function. $\tau(q)$ is obtained from the slope of the linear fittings performed in the selected regions of the partition function.

Notice that $D(q)$ exhibits multifractal behaviour when it is a monotonically decreasing function dependent on q. By contrast, it is considered monofractal when $D(q)$ is independent of q, i.e., it is represented by a horizontal straight line of constant slope. Another multifractal parameter used in this work is the degree of multifractality, $\Delta D(q) = D(q_{min}) - D(q_{max})$. This parameter indicates the multifractal strength of the image, i.e., the higher the $\Delta D(q)$ value, the greater the multifractality of the image. By contrast, the smaller the $\Delta D(q)$ value, the more monofractal it is.

In this work, we first propose to study the partition functions of each image establishing the scale ranges where the linear fits will be made to complete the analysis. Note that there will be a partition function for each of the channels that make up each colour profile. Subsequently, once the scale ranges have been established, the values of $D(q)$ are computed and depicted against q to obtain the generalised dimensions function. Finally, since Grey-Scale images are considered as reference images, comparisons are made with the different colour formats. For this purpose, the difference between the values of the Grey-Scale dimension functions and the dimension functions of each channel is evaluated. This difference allows to determine the channels and scale ranges that capture the multifractal behaviour of the original image and, therefore, determine which colour format and/or channel is more representative of each original image.

IV. Results and Discussion

In this section, the main findings after applying the box-counting and the method of moments to the image set are shown. First, the results of the analysis of the image of reference, i.e., the Grey-Scale, are presented followed by the RGB, CMYK, HSV and HSI formats. Finally, a comparison between the colour formats and the Grey-Scale images is accomplished.

A. Multifractal Analysis of Grey-Scale images

First of all, it should be noted that the box-couting method and the method of moments are used to carry out the multifractal analysis. Both are performed in Matlab software. In this case, for an image size of 128x128 pixels, the values of the scale (δ) range from $\delta = 2^0 = 1$ to $\delta = 2^7 = 128$. The values of the moments q are set between -4 and 4.

The partition functions of the three images selected and represented in Grey-Scale (see Figure 2) present similar shapes. Figure 4 (a) shows the partition function corresponding to the image of the area 1 of the board. However, it is representative of the rest of the Grey-Scale images. As observed, none of them show crossovers that distinguish scale ranges, i.e., a single linear region is observed from $\delta = 1$ to $\delta = 128$. In this way, the generalised dimensions function, $D(q)$, can be completely reconstructed for all moments q. Linear fits are performed with a coefficient R^2 greater than 0.99 for all cases. Figure 4 (b) shows the generalised dimensions function, $D(q)$,

Copyright (c) IARIA, 2023. ISBN: 978-1-68558-107-7

corresponding to the image of the area 1 of the board. Again, it is representative of the rest of the Grey-Scale images. As seen, the generalised dimension function is horizontal, thus it can be considered as a monofractal behaviour.

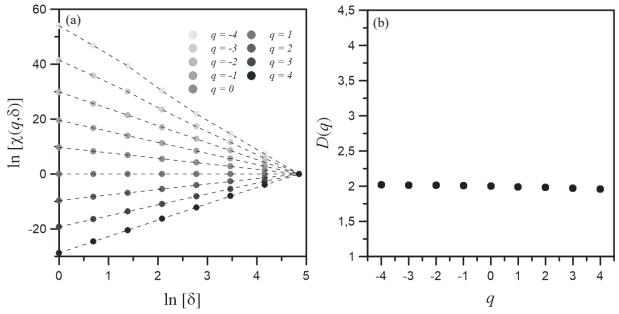

Figure 4. Graphs corresponding to the image of the area 1, (a) Partition function, (b) Generalised dimensions function.

Table I shows the results for the $D(q)$ of the three areas of the board. The values of $D(q)$ exhibit a very small degree of multifractality, so that, monofractal behaviour is considered in all three cases. It should be noted that the $\Delta D(q)$ of image area 1 is higher than in the rest of the images. This is due to the fact that the estimation for negative q values is worse. However, the rest of the function $D(q)$ is monofractal. Images of areas 2 and 3 are completely monofractal.

TABLE I. MULTIFRACTAL PARAMETERS OF THE 3 GREY-SCALE IMAGES

Degree of multifractality, $\Delta D(q)$	Image area 1	0.279
	Image area 2	0.059
	Image area 3	0.074

B. Multifractal Analysis of RGB images

In Figure 5, the partition functions obtained from the image of area 1 of the board for the 3 channels of the RGB colour profile are shown, as an example. In contrast to Grey-Scale images, the RGB images have different crossovers depending on the colour channel, so that there are different linear regions. Therefore, multifractal analysis is performed in different scale ranges depending on the colour channel. The same behaviour is observed for the RGB images of areas 2 and 3, i.e., depending on the image and the colour channel, partition functions with linear regions differing from each other are obtained.

Table II summarises the results obtained from the 3 RGB images analysed. On the one hand, the values of the degree of multifractality, $\Delta D(q)$, are presented. On the other hand, in order to detect which channel is capable of exhibiting the same monofractal behaviour as the reference Grey-Scale image (see Table I), the quadratic error ($\sum x^2 = \sum (D(q)_{gs} - D(q)_c)^2$) is estimated, which summarises the differences between the Grey-Scale and the colour channel. A value of the difference less than or equal to 0.2 is considered acceptable.

It should be noted that Table II indicates which colour channels do or do not exhibit scaling behaviour for a given range

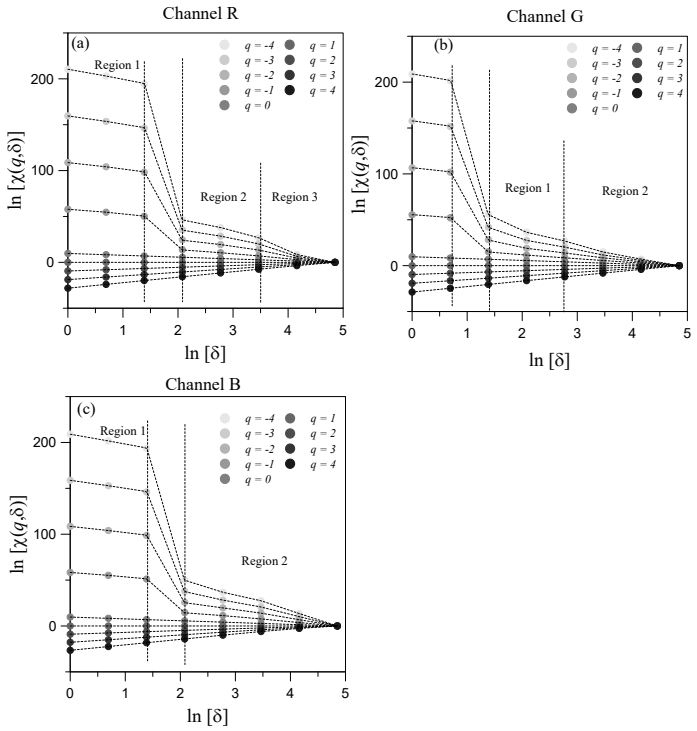

Figure 5. Partition functions of the RGB image of area 1, (a) Partition function of channel R, (b) Partition function of channel G, (c) Partition function of channel B. The crossovers for the linear fits have been made by vertical broken lines.

of scales. That is, scaling behaviour exists when the values of $D(q)$ are constant (monofractal) or decrease (multifractal) as the q moments grow. Increasing $D(q)$ functions implies a non-scaling behaviour. Therefore, regions which exhibit scaling behaviour are denoted by the symbol ✓, otherwise they are marked with $-$. In Table II, Scaling Behaviour is denoted as SB.

As it can be seen in Table II, only channel G presents a scaling behaviour in all the δ regions for the three images. For channel R, only one δ region of images 1 and 2 show scaling properties, as opposed to channel B, where only one δ region of images 1 and 3 do not show it. In terms of the $\sum x^2$, regions exhibiting the least difference compared to the Grey-Scale images are specified next: In G channel, region 2 ($\delta = 16 - 128$) for the image of area 1; region 1 ($\delta = 1 - 128$) for the image of area 2; and region 2 ($\delta = 16 - 128$) for the image of area 3. In channel B, only in the image of area 2, specifically in the region 2 ($\delta = 16 - 128$). In channel R, an adequate approximation to the multifractal behaviour of the Grey-Scale reference image is not achieved.

C. Multifractal Analysis of CMYK images

The partition functions of the CMYK image 1 area 1 are shown in Figure 6 as a representative example. As seen, the CMYK images also show different partition functions depending on the chosen colour channel. Each of the channels that make up the CMYK colour profile have different linear

TABLE II. MULTIFRACTAL PARAMETERS OF THE 3 RGB IMAGES. COMPARISON WITH THE GREY-SCALE REFERENCE IMAGES

Channel R		SB[a]	$\Delta D(q)$	$\sum x^2$
$\Delta D(q)$ Image 1	Reg. 1 $\delta = 1-4$	-	-	-
	Reg. 2 $\delta = 8-32$	-	-	-
	Reg. 3 $\delta = 32-128$	✓	2.051	6.363
$\Delta D(q)$ Image 2	Reg. 1 $\delta = 1-8$	-	-	-
	Reg. 2 $\delta = 16-128$	✓	2.400	8.150
$\Delta D(q)$ Image 3	Reg. 1 $\delta = 1-4$	-	-	-
	Reg. 2 $\delta = 8-32$	-	-	-
Channel G		SB[a]	$\Delta D(q)$	$\sum x^2$
$\Delta D(q)$ Image 1	Reg. 1 $\delta = 4-16$	✓	2.224	9.179
	Reg. 2 $\delta = 16-128$	✓	0.588	0.165
$\Delta D(q)$ Image 2	Reg. 1 $\delta = 1-128$	✓	0.072	0.001
$\Delta D(q)$ Image 3	Reg. 1 $\delta = 4-16$	✓	3.112	21.062
	Reg. 2 $\delta = 16-128$	✓	0.436	0.186
Channel B		SB[a]	$\Delta D(q)$	$\sum x^2$
$\Delta D(q)$ Image 1	Reg. 1 $\delta = 1-4$	-	-	-
	Reg. 2 $\delta = 8-128$	✓	1.862	4.937
$\Delta D(q)$ Image 2	Reg. 1 $\delta = 4-16$	✓	1.980	8.251
	Reg. 2 $\delta = 16-128$	✓	0.315	0.116
$\Delta D(q)$ Image 3	Reg. 1 $\delta = 1-4$	-	-	-
	Reg. 2 $\delta = 8-32$	✓	0.622	0.774

[a] SB: Scaling Behaviour

regions between them, so the multifractal analysis is performed in different scale ranges and, therefore, different results are obtained for each channel.

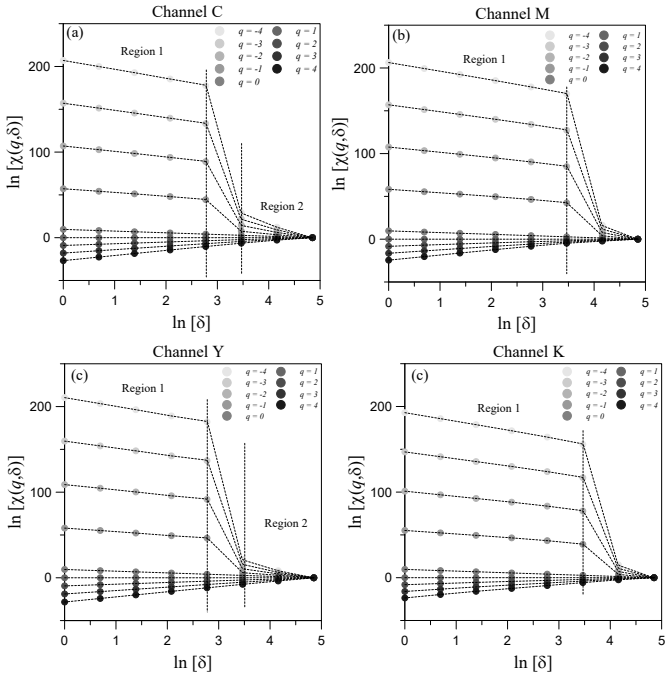

Figure 6. Partition functions of the CMYK image area 1, (a) Partition function of channel C, (b) Partition function of channel M, (c) Partition function of channel Y, (d) Partition function of channel K.

The same procedure used in the analysis of RGB images is explained next. First, it is determined which channel exhibits a scaling behaviour. In this case, with respect to channel C, the image of area 1 in region 2 ($\delta = 32-128$) shows a scaling behaviour, as well as the image of area 2 for the regions 1 ($\delta = 1-8$) and 2 ($\delta = 16-128$). On the other hand, no scaling features are found in the image area 3. In terms of channel M, only region 2 ($\delta = 32-128$) of the image of area 2 shows a scaling behaviour. In channel Y, both images 1 and 2, both in region 2 ($\delta = 32-128$), present scaling properties. Finally, in channel K, only the region 2 of image of area 2 ($\delta = 32-128$) exhibits a scaling behaviour.

Once the scale ranges where a scaling behaviour occurs have been established, a comparison with the Grey-Scale images is made. Only channel C can capture the scaling behaviour of the reference image, specifically in image area 2 for both scale ranges. In this case, it could be considered that the CMYK colour profile does not provide proper results, since it fails to capture the monofractality of the original image.

D. Multifractal Analysis of HSV images

The HSV images present the same behaviour as the previous ones, i.e., each of the images analysed shows different partition functions depending on the channel. In Figure 7, the partition functions of the HSV image area 1 are shown as a representative example. Again, as it can be seen, different linear regions and different scale ranges are obtained from the multifractal analysis.

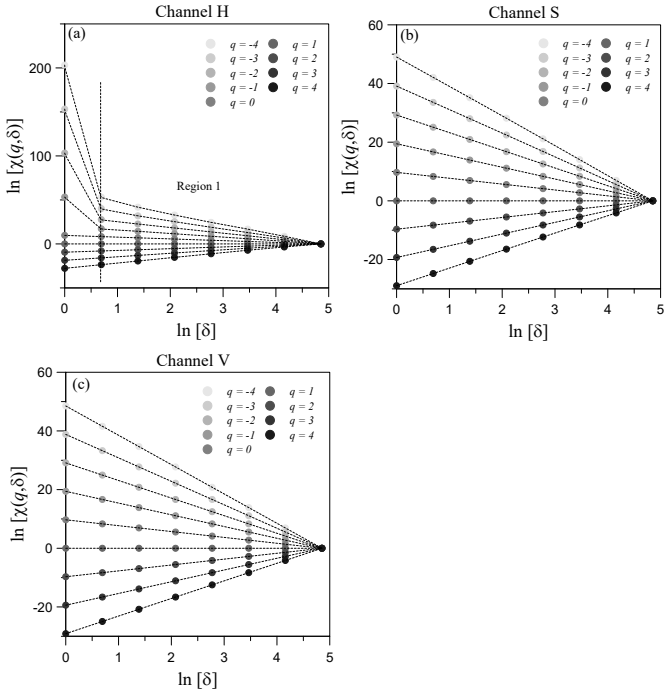

Figure 7. Partition functions of the HSV image area 1, (a) Partition function of channel H, (b) Partition function of channel S, (c) Partition function of channel V.

Next, the scale ranges that exhibit a scaling behaviour are explained. Regarding channel H, the 3 analysed images present scaling features in region 1, specifically from $\delta = 2$ to $\delta = 128$ for the image of areas 1 and 3, and from $\delta = 1$ to $\delta = 128$

for image area 2. The same result is found for channels S and V, where the images exhibit scaling properties for region 1 ($\delta = 1$ to $\delta = 128$).

In terms of the comparison with the Grey-Scale reference images, it is noteworthy to mention that all 3 channels are capable of capturing the scaling behaviour of the reference images, except in the case of image area 3 and channel H.

E. Multifractal Analysis of HSI images

Finally, the results obtained in the analysis of the HSI images are discussed. Again, for the same image, each colour channel has different linear regions (see Figure 8). This happens in the rest of images, as already discussed in the previous cases.

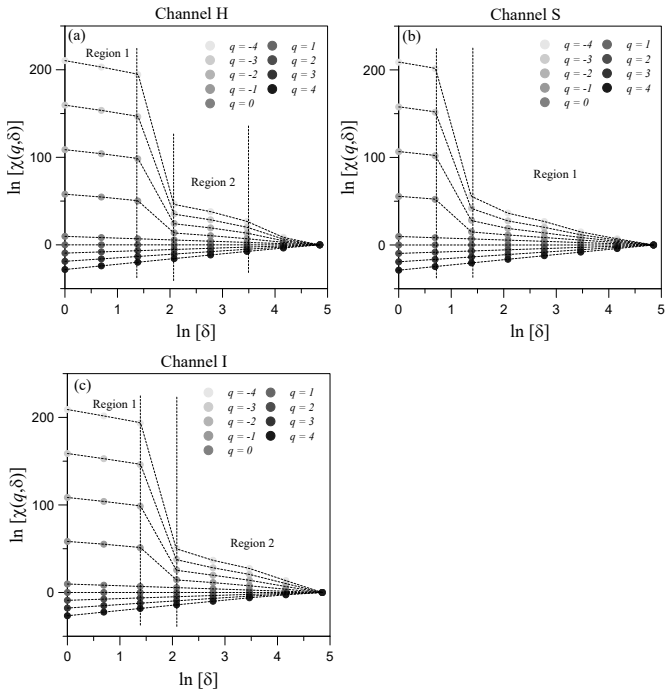

Figure 8. Partition functions of the HSI image area 1, (a) Partition function of channel H, (b) Partition function of channel S, (c) Partition function of channel I.

The scale ranges that exhibit a scaling behaviour are explained next: In channel H, the image of area 1 for a scale range from $\delta = 8$ to $\delta = 32$ in region 2, as well as image area 2 for the region 2 ($\delta = 16 - 128$), and image area 3 again in region 2 ($\delta = 8 - 32$). In channel S, a scaling behaviour is found in region 1 ($\delta = 4 - 128$) of the image of area 1, in the image of area 2 in region 1 ($\delta = 1 - 128$) and in the image of area 3 in regions 1 ($\delta = 4 - 16$) and 2 ($\delta = 16 - 128$). In I channel, image area 1 shows scaling features in region 2 ($\delta = 8 - 128$), the image area 2 in regions 1 ($\delta = 4 - 16$) and 2 ($\delta = 16 - 128$), and image of area 3 only in region 2 ($\delta = 8 - 32$).

Compared to the Grey-Scale reference images, it should be highlighted that channel H fails to capture the reference scaling behaviour in any of the images. Regarding channel S, the results are acceptable for the image of area 2, in region 1 ($\delta = 1 - 128$), and in image of area 3 in region 2 ($\delta = 16 - 128$). Finally, channel I only provides acceptable results for image area 2, specifically in region 2 ($\delta = 16 - 128$).

F. Comparison between Grey-Scale images and colour formats

The aim of this subsection is to summarise the colour channels that have been detected as the best approximation to the monofractal behaviour of the Grey-Scale reference images. In order to do so, the focus is on the difference between the $D(q)$ values of the Grey-Scale images and those of the colour models assessed with the quadratic error ($\sum x^2$). Table III shows how the colour channels resemble to the original image measured as percentage. This percentage is calculated by considering the colour channels that exhibit scaling behaviour and taking into account those whose quadratic error ($\sum x^2$) is less than or equal to 0.2. This way, those colour channels that have presented a lower error will have a higher percentage. That is, if a channel, in all cases, has managed to capture the monofractal behaviour of the reference image, it will have a percentage of 100% and, therefore, if it has not been able to capture such behaviour in any of the cases, it will be scored with 0%. Therefore, the higher the percentage value, the more representative and better approximation the channel presents. It should be noted that Table III shows the results of the three images analysed from an overall global approach.

TABLE III. APPROXIMATION BETWEEN GREY-SCALE REFERENCE IMAGES AND DIFFERENT COLOUR PROFILES IN PERCENTAGE

Colour profile		**Approximation rate** (%)
RGB	Channel R	0%
	Channel G	60%
	Channel B	25%
CMYK	Channel C	67%
	Channel M	0%
	Channel Y	0%
	Channel K	0%
HSV	Channel H	67%
	Channel S	100%
	Channel V	100%
HSI	Channel H	0%
	Channel S	50%
	Channel I	25%

As seen, three out of the four colour formats studied fail to capture the reference monofractal behaviour. For RGB, CMYK and HSI formats, there is at least one channel that can not be accepted as a proper approximation of the reference images, exhibiting a percentage of 0%. By contrast, there are other channels with an acceptable approximation with a percentage over 60%, e.g., channels G, C and S for RGB, CMYK and HSI, respectively. Finally, the HSV colour model provides proper results, since a high approximation (between 67% and 100%) is achieved for three channels and their three images.

V. CONCLUSIONS

This work proposes a novel methodology to analyse images in different colour formats: Grey-Scale, RGB, CMYK, HSV

and HSI by means of a multifractal approach based on the box-counting method and the method of moments. The study is carried out on thermal images of a Raspberry Pi3 electronic device.

Results show that the images in all the studied colour profiles have different partition functions as well as different scale ranges. This implies that the multifractal analysis varies depending on both the image format and the colour profile. In fact, the same image presents different multifractal behaviour depending on the colour format. On the contrary, the partition functions of the Grey-Scale images show linearity for all values of δ (1-128) in all images analysed.

The capability of capturing the behaviour of the original image of each format is evaluated by estimating the approximation of each colour channel with respect to the Grey-Scale image.

Results show that the CMYK colour profile is not considered suitable, as it fails to capture the multifractal behaviour of the original image in most of its channels. Among them some channels of RGB and HSI are able to approximate to the behaviour of the original image, the HSV arises as the most suitable format for analysing thermal images from a multifractal approach. Finally, it should also be noted that the capability to reproduce the monofractal behaviour of Grey-Scale images also depends on the range of scales considered (δ). For RGB and HSI formats, the scale range is usually from 16 to 128, so no monofractality can be found for scales ($\delta < 16$). Conversely, in the HSV format, the scale range covers the entire image with δ ranging from 1 to 128, so in this sense, this format is the one that exhibits monofractality over a larger range of scales.

The disparity of scaling behaviours found for different image channels and formats suggests an in-depth study on the multifractal features of images represented in different formats using the usual image analysis benchmarks from the literature is needed. As future work, it would be interesting to build a meta-model, in which different formats would consider their "understanding" of the image, while that meta-model would combine their "opinions".

ACKNOWLEDGMENT

Work supported by eFracWare project (TED2021-131880B-I00), funded by Spanish MCIN and the European Union "NextGenerationEU"/PRTR on MCIN/AEI/10.13039/501100011033, and eMob (PID2022-137858OB-I00), funded by Spanish MCIN/AEI/10.13039/501100011033/FEDER, UE.

REFERENCES

[1] B. Mandelbrot, "How long is the coast of britain? statistical self-similarity and fractional dimension," *Science*, vol. 156, pp. 636–638, 1967.

[2] A. N. Kravchenko, C. W. Boast, and D. G. Bullock, "Multifractal analysis of soil spatial variability," *Agronomy Journal*, vol. 91, no. 6, pp. 1033–1041, 1999.

[3] M. S. Jouini, S. Vega, and E. A. Mokhtar, "Multiscale characterization of pore spaces using multifractals analysis of scanning electronic microscopy images of carbonates," *Nonlinear Processes in Geophysics*, vol. 18, pp. 941–953, 2011.

[4] C. Evertsz and B. Mandelbrot, "Appendix b. multifractal measures. chaos fractals." *Springer*, pp. 922–953, 1992.

[5] M. Ivanovici and N. Richard, "Fractal dimension of color fractal images," *IEEE Trans. Image Processing*, vol. 20, pp. 227–235, 1 2011.

[6] S. R. Nayak, J. Mishra, A. Khandual, and G. Palai, "Fractal dimension of rgb color images," *Optik*, vol. 162, pp. 196–205, 6 2018.

[7] S. Verdú, J. Barat, and R. Grau, "Fresh-sliced tissue inspection: Characterization of pork and salmon composition based on fractal analytics," *Food and Bioproducts Processing*, vol. 116, pp. 20–29, 7 2019.

[8] J. Chauveau, D. Rousseau, P. Richard, and F. Chapeau-Blondeau, "Multifractal analysis of three-dimensional histogram from color images," *Chaos, Solitons and Fractals*, vol. 43, pp. 57–67, 2010.

[9] N. Reljin, M. Slavkovic-Ilic, C. Tapia, N. Cihoric, and S. Stankovic, "Multifractal-based nuclei segmentation in fish images," *Biomedical Microdevices*, vol. 19, no. 17, 9 2017.

[10] R. Uthayakumar and D. Easwaramoorthy, "Multifractal analysis in denoising of color images." IEEE, 2012, pp. 228–234.

[11] B. Mandelbrot, *The fractal geometry of nature*, 3rd ed. New York: W. H. Freeman and Comp., 1983.

[12] J. Feder, *Fractals*, ser. Physics of Solids and Liquids. Springer, 2013.

[13] P. Grassberger, "Generalized dimensions of strange attractors," *Phys. Lett. A*, vol. 97, no. 6, pp. 227–230, 1983.

[14] H. Hentschel and I. Procaccia, "The infinite number of generalized dimensions of fractals and strange attractors," *Physica 8D*, vol. 8, pp. 435–444, 1983.

Copyright (c) IARIA, 2023. ISBN: 978-1-68558-107-7

A Graphical Analysis of the Multimodal Public Transport Network – The Bay of Cadiz

Patricia Camacho Magriñán
University of Cadiz, Puerto Real, Spain
email: patricia.camachomagri@uca.es

Pablo Pavón Domínguez
University of Cadiz, Puerto Real, Spain
email: pablo.pavon@uca.es

Patricia Ruiz
University of Cadiz, Puerto Real, Spain
The University of Sydney, Sydney, Australia
email: patricia.ruiz@uca.es

***Abstract*—The structure of the current public transport network is the result of many different political, economical and societal decisions over a long period of time. Further developments of these networks require exhaustive analysis of the actual topology and its properties in order to achieve significant improvements. In this work, a statistical analysis and graph theory approach of the multimodal transport network of the Bay of Cadiz is proposed. First, the statistical characteristics of centrality and robustness of the global network are calculated. Later, the influence of specific means of transport on the complete public transport network is analyzed by comparing these parameters against different subnetworks where one or more transport networks have been eliminated. The results obtained evince the importance and influence of the different transport networks in the Bay of Cadiz, highlighting those presenting high robustness on the overall network, as well as those whose influence is limited.**

Index Terms*—Multimodal transport network; public transport efficiency; graph theory; centrality and robustness metrics.

I. Introduction

Society is currently experiencing the migration of population to big cities world wide. It is forecasted that by 2050 over 66 % of the population will live in urban areas [1]. This fact brings many opportunities but also many challenges that governments need to face to overcome traffic congestion, spatial inequalities and promote sustainability and economic development [2]. Among many other issues, an in-depth study of the Public Transport System (PTS) is essential for the development of cities to make them more efficient, sustainable and attractive to users, thus reducing traffic congestion, pollution or noise, and making cities more livable.

However, their design, planning and expansion of PTSs are not straightforward due to the demands of all actors involved. For example, quality of service and passenger comfort are essential to increase ridership. Low operational cost is required to make it profitable for the operator. Efficiency is required not only to reduce operational cost but also to address sustainability, as well as connectivity between different transport networks [3].

Public transport networks can be studied or assessed from different points of view, such as trip and route planning, user ease of use, or graph theory, among others [4]. In the latter, transport networks are represented as a graph, whose nodes and edges determine the shape and composition of the network. The nodes represent the transport stops; while the edges represent the route between stops.

Multimodal transport is defined as the process of transporting a person/goods between two distant points using two or more modes of transport. It is experiencing a great development around the world because of its high flexibility and efficiency and low cost and energy consumption [5]. In this work, we propose an analysis of the multimodal public transport network of the Bay of Cadiz, including train, tram, boat, urban and interurban bus networks. Different characteristic parameters of the network topology are obtained and compared against different subnetworks where not all the means of transport are presented. The results obtained demonstrate the level of network connectivity, as well as the effect of extracting one or more transport networks and the influence of such extraction. Thus, the relevance of each of them and the connections between the different stops of the targeted network are checked.

The remainder of the paper is structured as follows: the most relevant related works are briefly presented in Section II; the methodology used is introduced in Section III; Section IV shows the results obtained; and finally, Section V reflects the main conclusions and outlines some future research lines.

II. Related Works

The study of multimodal transport networks has been widely addressed in the literature. He et al. [6] study freight transport in the Netherlands, focusing on road, river and rail transport, obtaining a series of critical nodes essential for the stability of the network structure, thus obtaining the key areas of the network. Wang et al. [7] study the multimodal transport network of the China-Europe Railway Express, obtaining that the transfer between road and rail manages to alleviate the cascade failures that can occur. Tympakianaki et al. [8] study the effect of tunnel closures on the Stockholm transport network, resulting in the need for network redistribution to avoid traffic management problems for the city. Guo et al. [5] analyse the multimodal transport network of the Sichuan-Tibet (China) region of rail, road and air to place emergency rescue facilities, concluding that the whole network should be taken into account, especially at the most important nodes and links.

Graph theory has been also applied to analyze transport networks. In [9], the Madrid metro network is analysed through centrality and robustness parameters, focusing on closeness centrality and cluster coefficient. As a result, the

Copyright (c) IARIA, 2023. ISBN: 978-1-68558-107-7

vulnerability of the entire network is obtained, as well as the identification of the most important stops to achieve robustness in the network. Similarly, Mariñas Collado et al. [10] carried out a study of the Barcelona metro network using indicators of robustness, cluster coefficient and average efficiency. Thus, they obtained the characteristics of the different stops with the aim of obtaining a specific analysis to plan and restructure the network in search of better viability. Derrible makes use of graph theory in [11], to study the centrality of the metro network of various cities, focusing on centrality measures in search of future efficiency improvement for network planning and sustainable cities. Frutos Bernal et al. [12] analyze the Madrid metro network in terms of centrality measures to verify the location of the different stops, showing that the stops in the center of the city are those with greater centrality and, therefore, greater connection. Cats [13] analyzes the historical evolution of the multimodal rail transport network (tram, light rail, metro, high-speed express connections and local, suburban and regional trains), focusing on the efficiency and centrality of the nodes. In this way, it shows how it is affected by the technological factor in search of better connectivity, taking into account the increase in urban centres and population growth.

III. Methodology and Case of Study

The metropolitan area of the Bay of Cadiz comprises 12 municipalities, with a total of 823,806 inhabitants [14] [15]. These towns are: Cadiz (CA), El Puerto de Santa María (PSM), San Fernando (SF), Puerto Real (PR), Jerez de la Frontera (JF), Chiclana de la Frontera (CF), Rota (RO), Conil de la Frontera (CoF), Arcos de la Frontera (AF), Chipiona (CH), Sanlúcar de Barrameda (SB), and Medina Sidonia (MS). As it can be seen in Figure 1, they are all located in the province of Cadiz, south-west of Andalucia (Spain).

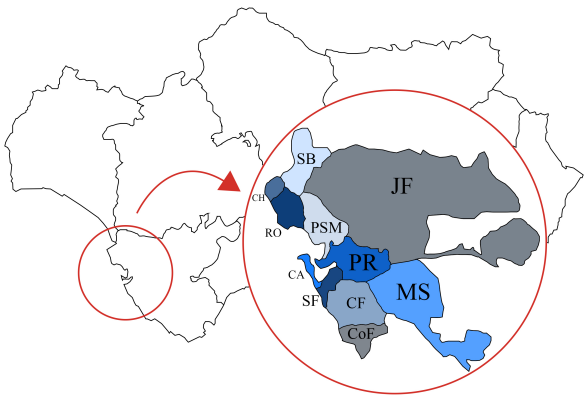

Fig. 1. Location of the municipalities that form the Bay of Cadiz in Andalusia, Spain.

These municipalities are scattered across the territory and require urban and interurban transport systems to interconnect them and meet passenger demands. The Transport Consortium of the Bay of Cadiz operates a transport network comprising train, boat, tram and bus services, both at urban and interurban level. The stops of the train, tram and boat networks are outward and return, thus providing two-way journeys. For the rest of the networks, any stop only refers to one way trip, because they are generally circular lines (see [15] [16] for more detailed information). Table I shows the different types of transport offered in each of the cities [16].

TABLE I
The different means of transport included in each of the transport networks for the twelve cities included in the metropolitan area of Bay of Cadiz

City	Pop.	Interurban	Urban	Train	Boat	Tram
CA	113066	✓	✓	✓	✓	✓
PSM	89435	✓	✓	✓	✓	
SF	94120	✓	✓	✓		✓
PR	41963	✓	✓	✓		
JF	212730	✓	✓	✓		
CF	87493	✓	✓			✓
RO	29491	✓	✓		✓	
CoF	23497	✓	✓			
AF	30953	✓	✓			
CH	19592	✓				
SB	69727	✓				
MS	11739	✓				

The representation of the public transport network of the Bay of Cadiz has been determined using the L-Space method initially proposed in [17] [18]. In this method, the nodes represent stops, while the edges represent the given connection between two nodes of a route. The multimodal transport network is represented as a directed graph $G = (V, E)$, where the set of nodes ($V = \{v_1, v_2, ..., v_N\}$) corresponds to the different transport stops, and the trips between any two stops correspond to the set of directed edges (E). The adjacency matrix of G, A_G is an asymmetric matrix of size N x N, where each entry a_{ij} equals 1 if there is a mean of transport that offers trip that goes from stop v_i to stop v_j, 0 otherwise. Figure 2 shows the resulting graph of the complete public transport network in the Bay of Cadiz using Matlab software.

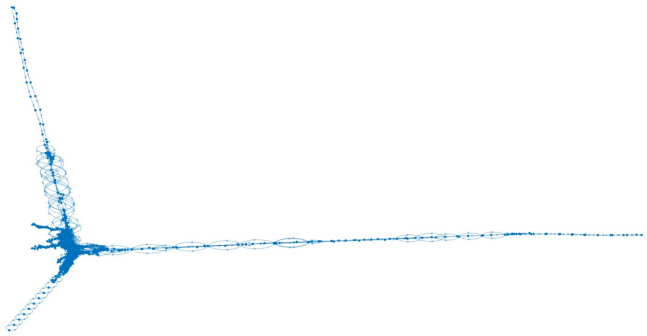

Fig. 2. Resulting graph of the complete public transport network in the Bay of Cadiz.

In order to study the relevance of the different modes of transport that constitute the multimodal network, a set of sub-networks has been created based on the combination of the different existing transports. Specifically, three categories or groups have been considered. They are explained next, and

Copyright (c) IARIA, 2023. ISBN: 978-1-68558-107-7

shown in Figure 3. Group A is composed of the different possible combinations that can be obtained from the different interurban networks of the set (train, tram, boat). Group B is related to the interurban bus network and two subgroups are possible. First, the global network is analyzed without the interurban network. Second, only the interurban is considered. Regarding group C, two possible subgroups are considered. On the one hand, all the means of transport are included except the urban bus networks for all cities. On the other hand, there are twelve subgroups C, one per each city whose urban network is not included.

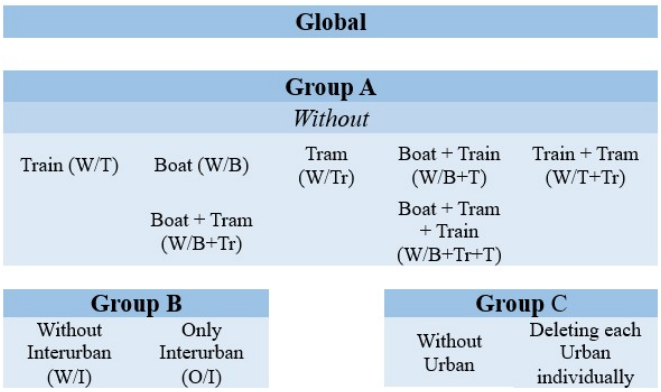

Fig. 3. Classification of Subgraph Groups. In brackets, abbreviation of each, where "W/" stands for "Without" and "O/" stands for "Only".

A. Statistical and robustness parameters

The analysis of a transport network involves examining specific data about its structure, including relevant statistical and robustness parameters [19] [20]. Next, the most relevant features analyzed in this work are presented:

- The *density (d)* of the network is a measure of the number of existing connections in relation to the total number of possible connections in the network.

$$d = \frac{E}{V(V-1)} \tag{1}$$

- The *frequency distribution of degree (P(k))* in a network assigns to each degree k the number of nodes that have that value, describing the proportion of nodes in the network with that value.

$$P(k) = \frac{V_k}{V} \tag{2}$$

  Where V_k is the number of nodes with degree k in the graph, and V is the total number of nodes given. Graphs with a more uniform *degree distribution* tend to have a higher *normalised robustness indicator* compared to those with a more heterogeneous distribution. The value of this is higher when more alternative routes are available, and lower when the system is larger.
- The *diameter (D)* of a graph is defined as the longest distance between any pair of nodes in the network, representing the longest path.
- The *closeness centrality* $C_c(i)$ is defined as the proximity to all other nodes in the graph. It is calculated as stated in (3), where $d_{(i,j)}$ is the shortest distance from node i to node j; while $d_{(j,i)}$ is the shortest distance from node j to node i.

$$C_c(i) = \frac{1}{\sum_{j \neq i}(d(i,j) + d(j,i))} \tag{3}$$

  Nodes with a higher closeness are considered more influential in the network, occupying a more central position. In this way, it is possible to identify those that are most relevant to the connection in the graph.
- The *betweenness centrality* (Bc_i), measures the degree to which a node is on the shortest path between other pairs of nodes in the network, i.e., the number of times a node acts as an intermediary in communication. It is calculated as stated in (4), where σ_{jk} is the total number of shortest paths between nodes j and k, and $\sigma_{jk}(i)$ is the number of such paths passing through node i.

$$Bc_i = \sum_{j \neq i \neq k} \frac{\sigma_{jk}(i)}{\sigma_{jk}} \tag{4}$$

  Nodes with high *betweenness centrality* occupy strategic positions in the network, so their removal can have a significant impact on the connectivity and efficiency of the network.
- The *average efficiency* ($E[\frac{1}{H}]$), represents the overall communication capacity of a network by calculating the average of the efficiencies of all the pairs of nodes that make it up as shown in (5), where $d(v_i, v_j)$ is the shortest path distance between nodes v_i and v_j of the network, using $\frac{1}{V(V-1)}$ as the normalisation factor.

$$E[\frac{1}{H}] = \frac{1}{V(V-1)} \sum_{i,j=1, i \neq j}^{V} \frac{1}{d(v_i, v_j)} \tag{5}$$

  The efficiency of a pair of nodes is defined as the inverse of the shortest distance between them. It ranges between 0 and 1. The higher the value of this parameter, the higher the robustness of the analysed network because it refers to the survivability against random failures or deliberate attacks involving the removal of nodes and links [20] [21].
- The *normalised robustness indicator* ($\bar{r}^T$), which ranges from 0 to 1, evaluates the resilience of a network to failures and its ability to maintain connectivity. $\bar{r}^T$ is given by the ratio between the number of alternative routes in the network and the total number of nodes [20], from the total number of edges E and the number of nodes V.

$$\bar{r}^T = \frac{ln(E - V + 2)}{ln(\frac{V(V-1)}{2}) - V + 2} \tag{6}$$

- The *global cluster coefficient parameter* (G_c) indicates how neighbours of a given node are connected to other nodes, ranging between values of 0 and 1.

$$G_c = \frac{1}{V}\sum_{i=1}^{V} G_c(v_i) \tag{7}$$

Where $G_c(v_i)$ represents the individual cluster coefficient of each node, while V means the total number of nodes. The *clustering coefficient* reflects the fault tolerance capability, so as the value of G_c increases, the local fault tolerance increases.

The use of the aforementioned statistical and robustness parameters, in addition to the basic statistical parameters of *standard deviation* σ applied to degree distribution, have been used to compare the subgraphs versus the global network. Thus, by extracting one or several transport networks, the relevance of each transport system on the global network is evaluated.

IV. Results and discussion

This section first presents an analysis of the global multimodal network and then evaluates the influence of each subgroup on the complete network once the following are extracted from it.

A. Analysis of the complete Multimodal Public Transport Network of the Bay of Cadiz

First of all, the *density d* of the network studied, indicates a poorly connected network according to (1), with this value being approximately 0.00183. In comparison with other national transport networks, such as the metro networks of Madrid and Barcelona, which have values of 0.009421 and 0.0157 respectively [9] [10], the connectivity of the Bay's multimodal transport network is lower. This result is reasonable because the targeted network is a multimodal transport network where more than one type of transport is studied.

In terms of the node degree, the studied multimodal network presents a highly variable value varying from 80 to 2. The *average degree* of the network is $\langle k \rangle \approx 4.867$, meaning that most of the nodes has a low degree value. In Figure 4, the *distribution degree* $P(k)$ is shown.

As it can be seen in Figure 4, most of the nodes are concentrated in the first grades, being connected to at least two nodes. This is the most frequent grade (about 60%) although the average is 4.867. It is followed by grade 4 with a little more than 20%, i.e. the stops with the possibility to change route. After that, the decrease in percentage for the following grades occurs from grade 10 onwards, being less than around 2%.

Table II shows the five nodes with the highest degree values. As it can be seen, the station of Jerez presents the highest value, 80. Indeed, this node is included in three different means of transport (urban, interurban and train) and in many different lines in each of them. Table II also shows that there are two more locations in the overall network with a high degree value: *Asdrubal Square* and *Puerta del Mar* in Cadiz (in both directions), the latter being where the Cadiz hospital is located.

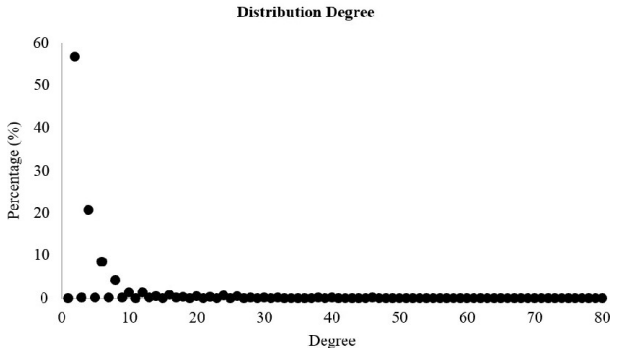

Fig. 4. Distribution Degree of the Public Transport network in the Bay of Cadiz.

TABLE II
Nodes with highest values of degree in the global multimodal transport graph of Bay of Cadiz

Node	Degree	Transport
Jerez Station	80	Interurban, Urban, Train
Asdrubal Square (to Cadiz)	70	Interurban, Urban
Puerta del Mar (to Cadiz)	64	Interurban, Urban
Puerta del Mar (from Cadiz)	60	Interurban, Urban
Asdrubal Square (from Cadiz)	58	Interurban, Urban

The diameter of the network is 73, representing the longest distance between any pair of nodes. However, the average shortest path is 19,622. In terms of the the centrality parameters, the *closeness and betweenness centrality* of each node forming the global network have been studied. The former reaches a maximum value of 0.090, shown in nodes such as *Telegrafia (to Cadiz), Puerta del Mar (the stop of the hospital* to Cadiz) and El Puerto Station (to Cadiz). The latter, i.e. the betweenness centrality, reaches a maximum value of 0.50 for *Jerez Station*, followed by values of 0.28 approximately, as in the nodes found in *El Puerto Station*. This makes the areas of Cadiz, PSM and Jerez, the most relevant in terms of centrality and, therefore, connectivity.

Regarding to the robustness parameters of the global network, the average *cluster coefficient* of the network is 0.031, a value similar to relevant networks such as the London Metro Network ($G_c = 0.0409$) or Tokyo Metro Network ($G_c = 0.0285$) [21] and, on Spanish territory, exceeding the Barcelona Metro Network ($G_c = 0.0044$) [10].

B. Transport system relevance on the multimodal network

The statistical parameters of groups A, B and C presented in Section III are summarised in Tables III, IV and V, respectively. These tables show the values of the different statistical and robustness parameters for each subgroup. These parameters are: *number of nodes, number of edges, diameter, average degree (k), standard deviation of the nodes' degree*

Copyright (c) IARIA, 2023. ISBN: 978-1-68558-107-7

(σ), cluster coefficient (G_c), average efficiency ($E[\frac{1}{H}]$) and normalised robustness indicator (r^T).

TABLE III
STATISTICAL PARAMETERS OF THE SEVEN DIFFERENT SUBGRAPHS INCLUDED IN GROUP A.

	Global	**W/T**	**W/B**	**W/Tr**
Nodes	1325	1323	1324	1310
Edges	3226	3202	3222	3186
Diameter	73	73	73	73
k	4.867	4.838	4.867	4.861
$\boldsymbol{\sigma}$ **Degree**	7.141	7.070	7.148	7.168
G_c	0.031	0.031	0.031	0.031
$E[\frac{1}{H}]$	0.032	0.032	0.032	0.032
r^T	0.986	0.986	0.986	0.986
	W/T+B	**W/T+Tr**	**W/B+Tr**	**W/T+B+Tr**
Nodes	1322	1304	1309	1303
Edges	3198	3162	3182	3158
Diameter	73	73	73	73
k	4.835	4.847	4.859	4.844
$\boldsymbol{\sigma}$ **Degree**	7.072	7.110	7.171	7.113
G_c	0.031	0.031	0.031	0.031
$E[\frac{1}{H}]$	0.032	0.032	0.032	0.032
r^T	0.986	0.986	0.986	0.986

In Table III, the statistical parameters of each of the seven subgraphs of group A are compared against the global network. This group considers maintaining the urban and interurban buses in all subgroups, but not considering the other means of transport in turns. As it is shown, there are no remarkable variations in any of the parameters studied. Indeed, the *diameter*, the *normalised robustness indicator*, the *clustering coefficient* as well as the *average efficiency* do not change in any of the studied subnetworks. In terms of the number of nodes and edges, the maximum variation is obviously found when not considering the combination of the three means of transport (W/T+B+Tr). However, when considering the deletion of a single mean of transport, the one presenting a higher impact is the tram. This is mainly because the stops and therefore, the links included in it, are exclusively for this kind of transport.

TABLE IV
STATISTICAL PARAMETERS OF THE TWO DIFFERENT SUBGRAPHS INCLUDED IN GROUP B.

	Global	**W/I**	**O/I**
Nodes	1325	1190	251
Edges	3226	1904	1322
Diameter	73	92	40
k	4.867	3.202	10.534
$\boldsymbol{\sigma}$ **Degree**	7.141	2.201	12.372
G_c	0.031	0.015	0.077
$E[\frac{1}{H}]$	0.032	0.015	0.082
r^T	0.986	0.990	0.879

The impact of the interurban bus network is analyzed in Table IV, where the parameters of the two different subgraphs that conform Group B are presented. It is observed that removing the interurban, subgraph (W/I), means losing a total of 135 nodes, a considerable loss, which highly affects all the statistical parameters of the subgraph, as it it is shown in Table IV. This means that some localities are disconnected from the rest of the graph, such as Chipiona, Sanlucar de Barrameda and Medina-Sidonia, and it makes more difficult the access to the rest of the network. Indeed, the value of the *diameter* has highly increased from 73 to 92. Thus, as this network has a smaller number of nodes than the global network, the *standard deviation* σ of the degree distribution is remarkably lower, showing that the distribution is more evenly distributed across the network nodes. In relation to the robustness parameters, it is observed that both the *average efficiency* $E[\frac{1}{H}]$ and the *clustering coefficient* are lower than the global network. In contrast, it has a similar value for the *normalized robustness indicator* r^T, indicating that it has a similar number of alternative routes as the global network.

Table IV also analyzes the interurban network by itself. It has a total of 251 nodes, differing greatly from the global network. On the one hand, its *diameter* is 40, so the distance between any two nodes is shorter compared to the global network. In terms of robustness parameters, the *normalized robustness indicator* r^T is close to the values of the other subgraphs in the group, so it has a similar number of alternative routes as the other graphs in this group. Regarding both *cluster coefficient parameter* G_C and *average efficiency* $E[\frac{1}{H}]$ present a remarkable increase in their values, indicating a higher robustness in this network.

TABLE V
STATISTICAL PARAMETERS OF THE TEN DIFFERENT SUBGRAPHS INCLUDED IN GROUP C.

	Global	**W/U**	**W/AF**	**W/CA**	**W/CF**	**W/CoF**
Nodes	1325	276	1270	1256	1214	1294
Edges	3226	1390	3151	3092	3116	3179
Diameter	73	41	73	73	73	73
k	4.867	10.072	4.962	4.924	5.008	4.913
$\boldsymbol{\sigma}$ **Degree**	7.141	12.098	7.261	7.085	7.405	7.207
G_c	0.031	0.073	0.030	0.032	0.033	0.031
$E[\frac{1}{H}]$	0.032	0.078	0.031	0.033	0.034	0.032
r^T	0.986	0.887	0.986	0.985	0.985	0.986
	Global	**W/PSM**	**W/JF**	**W/PR**	**W/RO**	**W/SF**
Nodes	1325	1193	877	1278	1227	1267
Edges	3226	2975	2470	3079	3079	3133
Diameter	73	73	66	73	64	73
k	4.867	4.987	5.633	4.818	5.019	4.946
$\boldsymbol{\sigma}$ **Degree**	7.141	7.334	8.279	7.203	7.378	7.285
C_c	0.031	0.033	0.042	0.029	0.033	0.029
$E[\frac{1}{H}]$	0.032	0.034	0.044	0.030	0.034	0.030
r^T	0.986	0.985	0.976	0.986	0.985	0.986

Finally, the parameters of subgraphs included in group C are shown in Table V. In this case the impact of the urban bus network is studied. As can be seen, the values obtained by removing a single urban network are similar to those of the overall network, having similar characteristics of nodes and edges, as well as in terms of robustness parameters. However, in the case of Jerez de la Frontera it is different. In this case, as it is the largest urban network of those studied, the effect of eliminating it is more significant in comparison with the rest.

Copyright (c) IARIA, 2023. ISBN: 978-1-68558-107-7

It is interesting to note the results obtained when all city buses are eliminated. It can be seen that the impact on the number of nodes and edges is high, as well as the *diameter* becomes smaller and, therefore, there are smaller maximum distances between nodes. Indeed, this behaviour is very similar to the subgroup of group B where only interurban bus network is considered. Both subgraphs present lower number of nodes, edges and diameter than the global network, but higher average degree and standard deviation, as well as similar values for the robustness parameters, meaning that both the interurban and urban networks are the most representative in the global graph.

This analysis shows that changes in the urban and interurban networks will directly influence the global network significantly, i.e. in terms of the robustness and connectivity. However, the tram, train and boat have a low impact. Moreover, independently of the studied subgraph, the *normalized robustness indicator* keeps a high value, highlighting the resilience of the network (in terms of connectivity) to failures.

V. Conclusions

In this work, a graphical analysis of graph theory has been carried out on the public transport network of the Bay of Cadiz, since it is a transport network that is in continuous growth and can give rise to studies on its efficiency. In order to achieve the objectives of this study, a statistical and graph theory analysis of the network structure is carried out. The global network has been partitioned in different graphs and subgraphs in order to analyze the influence of the different means of transport composing it.

The results of this work show the importance or influence of the different types of transport in the Bay of Cadiz. In this way, the networks that function as the core of the overall network are both the urban and the interurban bus networks. The interurban network presents the highest *normalised robustness indicator* as it is the one that connects the different localities included in the Bay of Cadiz. Some of them become isolated when this subnetwork is not considered. However, it is worth noting that in any of the studied subnetworks, the *normalised robustness indicator* presents a high value (always over 0.87) even when not considering many of the transport modes, meaning that the system is resilient and it maintains connectivity in case of failure of any transport mode.

As future work, the travel time or fuel consumption will be considered, including these features as weights in the network. In addition, a multifractal study of the Bay of Cadiz transport network based on the statistical study can provide more information in this respect, as well as studying how to adapt fractal algorithms to directed graphs of the different types of transport.

Acknowledgment

This work was supported by the project eFracWare (TED2021-131880B-I00) funded by Spanish MCIN and the European Union "NextGenerationEU"/PRTR on MCIN/AEI/10.13039/501100011033, and the project eMob (PID2022-137858OB-I00) funded by Spanish MCIN, and the Agency and the European Regional Development on MCIN/AEI/10.13039/501100011033/FEDER, UE.

References

[1] U. Nations, "Un-habitat," Retrieved: 06, 2023. [Online]. Available: https://unhabitat.org/topic/urban-planning

[2] European Strategy and Policy Analysis System (ESPAS), "Global Trends to 2030: The Future of Urbanization and Megacities," *ESPAS Ideas*, 2019.

[3] J. Malasek, "A set of tools for making urban transport more sustainable," *Transportation Research Procedia*, vol. 14, pp. 876–885, 2016.

[4] J. Zhang, F. Liao, T. Arentze, and H. Timmermans, "A multimodal transport network model for advanced traveler information systems," *Procedia - Social and Behavioral Sciences*, vol. 20, pp. 313–322, 2011.

[5] J. Guo, Q. Du, and Z. He, "A method to improve the resilience of multimodal transport network: Location selection strategy of emergency rescue facilities," *Computers & Industrial Engineering*, vol. 161, pp. 1–15, 2021.

[6] Z. He, K. Navneet, W. van Dam, and P. Van Mieghem, "Robustness assessment of multimodal freight transport networks," *Reliability Engineering & System Safety*, vol. 207, p. 107315, 2021.

[7] B. Wang, Q. Su, and K. S. Chin, "Vulnerability assessment of china–europe railway express multimodal transport network under cascading failures," *Physica A: Statistical Mechanics and its Applications*, vol. 584, no. C, pp. 11–36, 2021.

[8] A. Tympakianaki, H. Koutsopoulos, E. Jenelius, and M. Cebecauer, "Impact analysis of transport network disruptions using multimodal data: A case study for tunnel closures in stockholm," *Case Studies on Transport Policy*, vol. 6, 2018.

[9] E. Frutos Bernal and A. Martín del Rey, "Study of the structural and robustness characteristics of madrid metro network," *Sustainability*, vol. 11, no. 12, 2019.

[10] I. Mariñas-Collado, E. Frutos Bernal, M. T. Santos Martin, A. Martín del Rey, R. Casado Vara, and A. B. Gil-González, "A mathematical study of barcelona metro network," *Electronics*, vol. 10, no. 5, 2021.

[11] S. Derrible, "Network centrality of metro systems," *PLOS ONE*, vol. 7, pp. 1–10, 2012.

[12] E. Frutos Bernal, A. Martín del Rey, and P. Galindo Villardón, "Analysis of madrid metro network: From structural to hj-biplot perspective," *Applied Sciences*, vol. 10, no. 16, 2020.

[13] O. Cats, "Topological evolution of a metropolitan rail transport network: The case of stockholm," *Journal of Transport Geography*, vol. 62, pp. 172–183, 2017.

[14] INE, "National Statistical Institute," Retrieved: 06,2023. [Online]. Available: https://www.ine.es/nomen2/index.do

[15] CTBC, "Bay of Cadiz Transport Consortium," Retrieved: 06, 2023. [Online]. Available: https://cmtbc.es/generica.php?pagina=creacion-y-objetivos

[16] Junta de Andalucía, "Junta de Andalucía. (Bay of Cadiz Metropolitan Transport Plan. Mobility Plan," Retrieved: 06, 2023. [Online]. Available: http://www.juntadeandalucia.es/medioambiente/portal_web/web/temas_ambientales/evaluacion_integracion_planificacion/evaluacion_ambiental/evaluacion_planes_programas/otros_planes_programas/PTM_Bahia_Cadiz/documentos/18132_06_15_3_Documento_Sintesis.pdf

[17] S. Porta, P. Crucitti, and V. Latora, "The network analysis of urban streets: A primal approach," *Environment and Planning B: Planning and Design*, vol. 33, no. 5, pp. 705–725, 2006.

[18] ——, "The network analysis of urban streets: A dual approach," *Physica A: Statistical Mechanics and its Applications*, vol. 369, no. 2, pp. 853–866, 2006.

[19] A. L. Barabási, "Network Science," Retrieved: 06, 2023. [Online]. Available: http://networksciencebook.com/

[20] Z. Ali and S. Bhaskar, "Basic statistical tools in research and data analysis," *Indian Journal of Anaesthesia*, vol. 60, p. 662, 2016.

[21] X. Wu, C. K. Tse, H. Dong, I. W. H. Ho, and F. C. Lau, "A Network Analysis of World's Metro Systems," in *Proceedings of the 2016 International Symposium on Nonlinear Theory and its Applications (NOLTA2016)*. The Institute of Electronics, Information and Communication Engineers, 2016, pp. 606–609.

Copyright (c) IARIA, 2023. ISBN: 978-1-68558-107-7

A Survey of Recent Applications of the PISALE Code and PDE Framework

Alice Koniges
Information and Computer Sciences
University of Hawai'i at Mānoa
Honolulu, HI, USA
email: koniges@hawaii.edu

David Eder
Physics and Astronomy
University of Hawai'i at Mānoa
Honolulu, HI, USA
email: dceder@hawaii.edu

Jonghyun Lee
Civil & Env Eng and Water Res Center
University of Hawai'i at Mānoa
Honolulu, HI, USA
email: jonghyun.harry.lee@hawaii.edu

Aaron Fisher
Information Technology Services
University of Hawai'i at Mānoa
Honolulu, HI, USA
email: fallen@andcheese.org

Yuriy Mileyko
Mathematics
University of Hawai'i at Mānoa
Honolulu, HI, USA
email: ymileyko@hawaii.edu

Monique Chyba
Mathematics
University of Hawai'i at Mānoa
Honolulu, HI, USA
email: chyba@hawaii.edu

Jack McKee
Mathematics
University of Hawai'i at Mānoa
Honolulu, HI, USA
email: jmckee@math.hawaii.edu

Young-Ho Seo
Civil & Env Eng and Water Res Center
University of Hawai'i at Mānoa
Honolulu, HI, USA
email: yhseo@hawaii.edu

Peter Yip
Aerospace Engineering and Mechanics
University of Minnesota
Minneapolis, MN, USA
email: yipxx043@umn.edu

Thomas Schwartzentruber
Aerospace Engineering and Mechanics
University of Minnesota
Minneapolis, MN, USA
email: schwart@umn.edu

Claudia Parisuaña
Department of Mechanical Engineering
Stanford University
Stanford, CA USA
email: cparisua@stanford.edu

Siegfried Glenzer
SLAC National Accelerator Laboratory
Stanford University
Menlo Park, CA USA
email: glenzer@slac.stanford.edu

***Abstract*—We review the basic equations, numerical solution techniques, and new application areas of a novel multi-purpose computer code framework, PISALE, for the solution of complex Partial Differential Equation (PDE) systems on modern computing platforms. We describe how the code solves equations in the fluid approximation using a novel combination of Arbitrary Lagrangian Eulerian (ALE) and Adaptive Mesh Refinement (AMR) methods. Sample problems from areas of ground water flow, high-speed impacts, and X-ray Free Electron Laser (XFEL) experiments are given.**

Keywords*—*Adaptive Mesh Refinement; Computational Fluid Dynamics; Arbitrary Lagrangian Eulerian Methods; Volume of Fluid; High Performance Computing; Surface Tension; Ground Water Flow.

I. Introduction

The PISALE codebase contains a Partial Differential Equation (PDE) solver framework based on the combined methods of Arbitrary Lagrangian Eulerian (ALE) dynamics and structured Adaptive Mesh Refinement (AMR). The PISALE code uses an explicit time-marching Lagrange step to advance the flow-field through a physical time step. The optional second phase involves a modification of the grid and a remapping (interpolation) of the solution to the new grid. The solution of PDEs on modern High Performance Computing (HPC) platforms is essential to the continued success of research and modeling for a wide variety of areas. The PISALE code name comes from the acronym Pacific Island Structured-AMR with ALE. In some earlier papers (e.g., [10]) the code is called ALE-AMR as it was one of the first codes to combine those two methods. There are several branches of PISALE to deal with disparate applications. These applications range from high energy density physics problems to geothermal flows. In this paper, we detail some of the wide variety of applications suitable for modeling with PISALE and discuss recent improvements to the code base.

In Section II, we give an overview of the equations used in the PISALE code. In Subsection II-A, we describe how the different physics modules are coupled using operator splitting. We also provide some additional information on the surface tension modules used in PISALE. In Section III, we give a summary of past PISALE applications followed by discussion on modeling groundwater flow in Subsection III-A. We then discuss recent hypervelocity impacts simulations with a comparison of PISALE results with experimental data and with results from other codes in Subsection III-B. The third new application is discussed in Subsection III-C, where we describe the modeling of droplet dynamics. We provide some conclusions and comments on future work in Section IV.

Copyright (c) IARIA, 2023. ISBN: 978-1-68558-107-7

II. PISALE EQUATIONS

The numerical methodology of PISALE was initially developed for pure gas dynamics and its novelty at the time was based on the coupling of AMR with a Lagrangian formulation that retains accuracy in standard two- and three-dimension problems, such as Sedov blast wave simulations [1]. By adding a complex Right Hand Side (RHS) to the basic gas dynamics with elastic/plastic flow terms, we are able to use operator splitting methods to model an extremely diverse variety of physical processes, each affecting the dynamically evolving fields at successive time intervals according to timescales. An example of a complex RHS is the use of anisotropic material failure models with material history in multi-material problems. Unlike the first implementations of these numerical techniques such as Wilkins [26], PISALE was written from the ground-up to be modular and take advantage of parallelism opportunities on HPC platforms. PISALE operates on top of the Structured AMR Application Interface (SAMRAI) library [8] and contains a general purpose PDE solver that uses a staggered-grid, Lagrangian formulation, written for coupled plasma/fluids with position and velocity being nodal variables and density, internal energy, temperature, pressure, strain, and stress being zonal (cell centered) variables. This basic solver is primarily for equations that can be written in conservation form and uses a volume of fluid approach. Thermal conduction and radiation transport coupled to the basic conservation law equations are solved by implementing the diffusion approximation, which uses a nodal radiation energy and a zone-averaged nodal temperature. These plasma/fluid equations in a Lagrangian formulation (in vector and indicial notation $i, j, k = 1, 2, 3$) are:

$$\frac{\mathrm{D}\rho}{\mathrm{D}t} = -\rho\nabla\cdot\vec{U} = \rho U_{i,i} \quad (1)$$

$$\frac{\mathrm{D}\vec{U}}{\mathrm{D}t} = \frac{1}{\rho}\nabla\cdot\boldsymbol{\sigma} = \frac{1}{\rho}\sigma_{ij,j} \quad (2)$$

$$\frac{\mathrm{D}e}{\mathrm{D}t} = \frac{1}{\rho}V\boldsymbol{s}:\dot{\boldsymbol{\varepsilon}} - P\dot{V} = \frac{1}{\rho}V\left(s_{ij}\dot{\varepsilon}_{ij}\right) - P\dot{V} \quad (3)$$

where $\frac{\mathrm{D}}{\mathrm{D}t} = \frac{\partial}{\partial t} + \vec{U}\cdot\nabla$ is the substantial derivative, ρ is the density, $\vec{U} = (u, v, w)$ is the material velocity, t is time, $\boldsymbol{\sigma}$ is the total stress tensor, P is the pressure, e is the internal energy, V is the relative volume ($\rho V = \rho_0$ where ρ_0 is the reference density), $\boldsymbol{s}$ is the deviatoric stress defined as $s_{ij} = \sigma_{ij} + P\delta_{ij}$ where δ is the Kronecker delta and $\dot{\boldsymbol{\varepsilon}}$ is the strain rate tensor. PISALE has a range of different strength and failure models that can be used for impact and other applications.

A. PISALE Physics Modules

PISALE has significant physical modeling capabilities in addition to the core ALE hydrodynamics and structural mechanics. These capabilities are provided through a flexible physics module system which allows their PDEs to be updated separately from the hydrodynamic models with a classical operator splitting scheme. Field variables in these physics modules are advanced in time after the hydrodynamic time step and the modules have hooks that allow them to update the field quantities when the ALE hydrodynamics alters the underlying mesh. Physical models provided in this manner include a laser ray tracing package [14], various surface tension models [11] [12], heat conduction, and diffusion-based radiation transport [7].

PISALE includes infrastructure to lower the barriers for the introduction of additional physics modules. Currently, this includes tools for transforming data and meshes from a block structured format to an unstructured indexing format, tools for tracing rays through meshes, and a basic Finite Element Method (FEM) framework for discretizing PDEs, see Figure 1. Field data in PISALE physics modules is updated after the ALE hydrodynamics step is complete. First field data is collected from the SAMRAI patch-AMR hierarchy into a parallel composite mesh, which can be utilized with unstructured solvers. Then FEM-based PDE discretizations are applied on the composite mesh to update the relevant field data. The updated field data on the composite mesh is then transformed back into the patch-AMR hierarchy. This approach enables the development of external solvers for PISALE without requiring the data to be represented as a SAMRAI patch hierarchy.

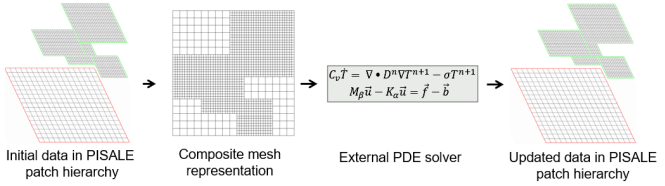

Fig. 1. Field data on PISALE patch mesh is transferred to composite mesh prior to solution by external PDE solver and then updated on patch mesh.

The current PISALE FEM framework includes only first order H^1 quadrilateral and hexahedron elements in 2D and 3D. This works well for the diffusion equation solvers utilized in the heat conduction and radiation diffusion modules. We are exploring the addition of elements from the $H(curl)$, $H(div)$, and L^2 spaces that would open up a path to discretizing a wider array of PDEs in topic as diverse as: plasma physics, mesoscale material modeling, seismicity in geophysics, and electromagnetics. The current FEM framework in PISALE only supports AMR in 2D. We are exploring FEM frameworks with 3D AMR capability that would improve the existing heat conduction, radiation diffusion, and surface tension models in PISALE. Some examples are Modular Finite Element Methods (MFEM) library [16] and the Multiphysics Object-Oriented Simulation Environment (MOOSE) [17].

1) Surface Tension: A major use case of the operator splitting system is the surface tension package, which models 2D and 3D surface tension using a multi-fluid Volume-of-Fluid (VOF) paradigm[4]. The VOF paradigm avoids tracking an explicit representation of fluid boundaries, instead reconstructing them at each time step based on the relative volume fractions of each fluid within every cell. This was chosen because volume fractions are already a core aspect of PISALE's multi-material formulation, meaning the surface tension package

Copyright (c) IARIA, 2023. ISBN: 978-1-68558-107-7

only needs to generate and apply a body force. A height function for each fluid is generated by summing up relative volume fractions along columns of a 3x5 or 3x3x5 stencil. Orientation and position of the stencil is chosen so that the interface is always in the central cell of the stencil, the fluid body is always on the "bottom" of the stencil, and the first derivatives of the height function are minimized. See Figure 2.

In 2D, three points are chosen based on the height function and mapped back to real coordinates, where they are used to generate a three-point circular fit of the boundary, which approximates an osculating circle. This scheme is robust to nonlinear meshes with regular column widths, but a correction term must be applied in the case of irregular column widths[15]. A circular fit of this kind can be shown second-order accurate when the mesh is regular enough[3], although is only first-order accurate when the mesh is non-orthogonal or nonlinear. Because the calculation of surface tension does not rely on mesh regularity, surface tension can be incorporated as a body force during Lagrangian time steps, allowing full ALE simulations with properly coupled surface tension effects.

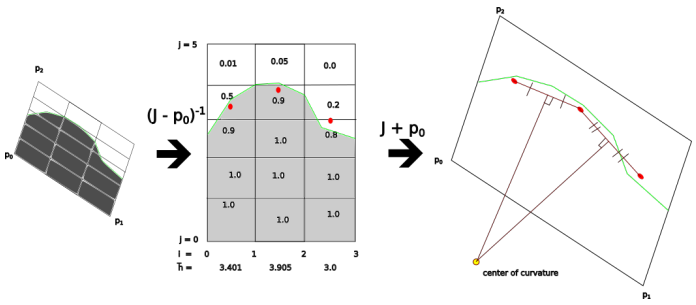

Fig. 2. Visual depiction of surface tension calculation using height functions in 2D.

In 3D, six points are chosen for a linear least-squares polynomial fit of the boundary with a quadratic polynomial $P(i, j)$ of the logical coordinates[12]. The polynomial's derivatives are then mapped through the mesh Jacobian to find first and second derivatives of the corresponding approximate parameterization $p(x, y)$ in real coordinates, which are used to calculate the mean curvature of the surface. Since the current 3D curvature calculation relies on a linear approximation of the mesh, the surface tension force can only be applied after the remap phase, and with mesh adaptation disabled.

III. Recent Applications Areas

PISALE has been applied to a wide range of applications. One early application was the protection of optics and diagnostics at the National Ignition Facility (NIF) and other large laser facilities [6]. It was also used to model ion heating experiments at Neutralized Drift Compression Experiment-II (NDCX-II) to study Warm Dense Matter (WDM) properties [2]. One of the early applications that used the surface tension capability of the code was modeling the dynamics of tin droplets for extreme ultraviolet (EUV) lithography [22]. Our recent applications include groundwater flow simulations for Hawaiian aquifers[23], impacts of particulates and rain droplets on hypersonic vehicles[27], and a range of experiments at Stanford Linear Accelerator Center (SLAC), a Department of Energy (DOE) Office of Science User Facility. Experiments include X-ray Free Electron Laser (XFEL) beam heating of hydrogen and water droplets[18] and interaction of laser produced proton beams with different materials. We summarize recent work in these three new application areas.

A. Groundwater Flow and Transport in Pacific Islands

Density-dependent miscible seawater-freshwater systems in island aquifers have been previously modeled with finite element or finite volume methods in an Eulerian framework. These simulations however, are deemed inadequate due to inappropriate grids and problems with scalability. Due to the density dependency, the governing Darcy-type flow equation is nonlinearly coupled with the mass and/or heat transport equations with a constitutive relationship, $\rho = \rho(p, T, c)$ where ρ is the density, p is the pressure, T is the temperature, and c is the salinity.

For seawater-freshwater simulation in the subsurface, the isothermal assumption, e.g., $\rho = \rho(c)$ under Boussinesq approximation is typically used for coupled flow and transport with appropriate boundary conditions [5]:

$$\nabla \cdot \mathbf{q} = 0 \tag{4}$$

$$\mathbf{q} = -\frac{\rho_0 g \mathbf{k}}{\mu}\left(\frac{\nabla p}{\rho_0 g} + \frac{\rho - \rho_0}{\rho_0}\nabla z\right) \tag{5}$$

$$\phi\frac{\partial c}{\partial t} + \nabla \cdot (\mathbf{q}c - \phi \mathbf{D}_{\text{eff}} \nabla c) = 0 \tag{6}$$

where $\mathbf{q}$ is the fluid flux, ρ_0 is the density at the reference c and T, g is the gravity constant, $\mathbf{k}$ is the permeability tensor of the porous medium, μ is the dynamic viscosity, ϕ is the porosity, and $\mathbf{D}_{\text{eff}}$ is the dispersion coefficient tensor.

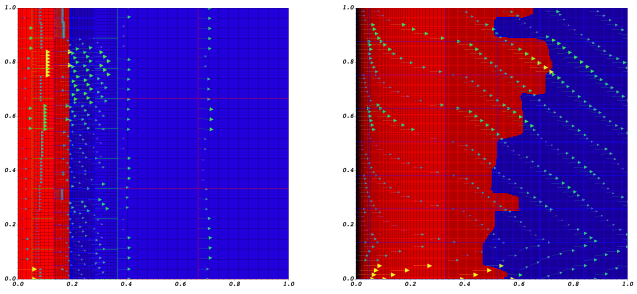

Fig. 3. Conservative tracer transport with heterogeneous hydraulic conductivity field at t = 0 yr (left) and 37.8 yrs (right).

A critical previously unaddressed challenge is the simulation of salinity transport in a large-scale aquifer with a spatially heterogeneous permeability field. Typically, and unsatisfactorily, coarse meshes with large diffusion coefficients (i.e., dispersivities) are implemented as numerical compromises at the cost of overestimated mixing physics. The simulated groundwater flow velocities are then used for reactive transport

Copyright (c) IARIA, 2023. ISBN: 978-1-68558-107-7

modeling, which often leads to the underestimated residence time of contaminant plumes and associated overly promising groundwater remediation decisions with increasing risks of cleanup operation failure. The flexibility of PISALE, with its ability to define interfaces and the use of AMR to dynamically define the grid, addresses these issues as shown in Figure 3. We show convective tracer transport with a heterogeneous hydraulic conductivity field and its corresponding groundwater velocity. Additionally, PISALE generally reduces simulation time to a tractable problem via the parallel HPC performance of the underlying scalable SAMRAI library.

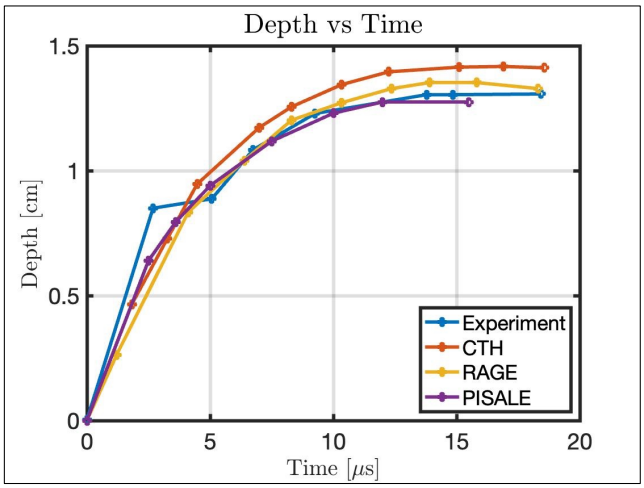

Fig. 4. Recent comparison of PISALE results with two openly published results from large code efforts (neither is open source) and experimental impact data.

B. Hypervelocity impacts

Impacts by particulates and rain droplets on hypersonic (Mach 5 and above) vehicles pose a major concern for safety of flight. It is understood that particulates of even micron-size are capable of impacting the surface quality of the vehicle [9]. Therefore, larger particles are likely to induce more surface damage and additional material erosion. To make the result more complex, the particles must traverse a shock discontinuity formed from hypersonic flight. As a particle traverses the shock, the post-shock conditions may result in a pressure, density, and temperature differential that leads to a spatio-temporal dependent particle shape change prior to making contact with the surface. PISALE offers the capability to capture such high-rate loading in a computationally cost effective manner with the implementation of AMR. PISALE has been verified and validated in its ability to capture hypervelocity impact phenomena of well-characterized ductile metals. Figure 4 shows impact crater depth in Al 6061-T6 as a function of time caused by an aluminum projectile with PISALE results in excellent agreement with experimental data [20]. The projectile has a diameter of $6.35mm$ and a velocity of 7 km/s. Figure 5 shows the PISALE simulation of the impact at three times.

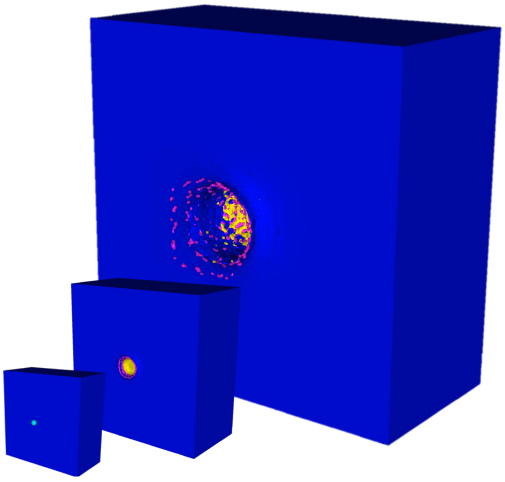

Fig. 5. PISALE simulation showing time of impact and crater at 5 and 15 μs.

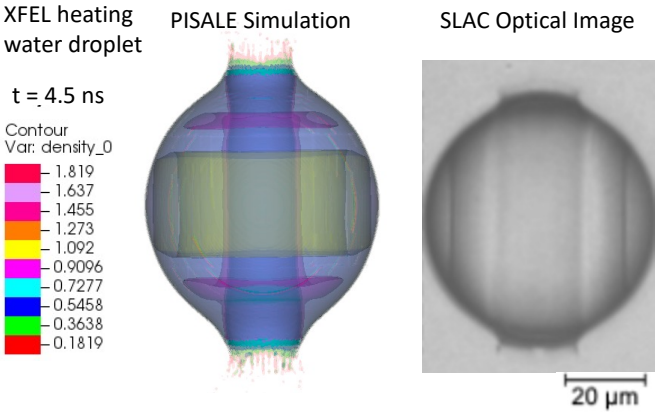

Fig. 6. Comparison of PISALE simulation of a water droplet heated by an XFEL with experimental image.

C. Modeling of SLAC experiments using XFEL beams

XFEL beams can be used to produce and study matter under extreme conditions. Liquids provide a means of bringing samples into the path of the X-ray beam for analysis. Ultrabright x-rays can blow up samples within a tiny fraction of a second, and modeling the dynamics of this interaction is critical to understanding which droplets can be used to collect data. These ultrashort ($\sim$ 50 fs), high energy ($\sim$ 8 keV), coherent x-ray sources can be used to both heat and probe targets. We discuss some recent results in modeling XFEL heating of water and hydrogen droplets. Figure 6 shows early time dynamics from a 3D PISALE simulation of a water droplet heated by an XFEL beam with a comparison to an experimental optical image [24] at the Coherent X-ray Imaging (CXI) instrument at SLAC. Previous work [19] modeling early stages of liquid-water-drop explosion showed 1D and 2D results assuming axisymmetry. This assumption is broken for later times due to distortions of the cavity boundary [19]. Therefore, the need of a 3D simulation not only as a diagnostic tool for early times,

Copyright (c) IARIA, 2023. ISBN: 978-1-68558-107-7

but also for modeling reflection and spallation mechanisms that lead to fragmentation and expansion observed in water under extreme conditions at later times [25].

The need for High Repetition Rate (HRR) targets in High Energy Density Science has been stated many times as the areas moves towards HRR facilities [21] [13]. When using droplets as HRR targets, fratricide can occur. This is caused by the explosion of a heated droplet impacting the following droplet, which can make it ineffective for the following shot. The need to skip this perturbed droplet causes a reduction in the effective repetition rate and data acquisition quality. Figure 7 shows a 3D PISALE simulation of three hydrogen droplets with the first droplet (lowest in the image) already exploded after being heated by an XFEL beam. The image is 9 ns after the XFEL beam passes through the first droplet. The resulting explosion creates debris seen impacting the following droplets. The middle droplet is clearly perturbed by the debris causing a reduction of the effective repetition rate factor of this target system by at least by factor of 2 because this perturbed droplet cannot be used as a target. The XFEL beam travels along the x-axis, which passes through the center of the lowest droplet. The orientation (not the location) of the three axes is shown for the inline and side views.

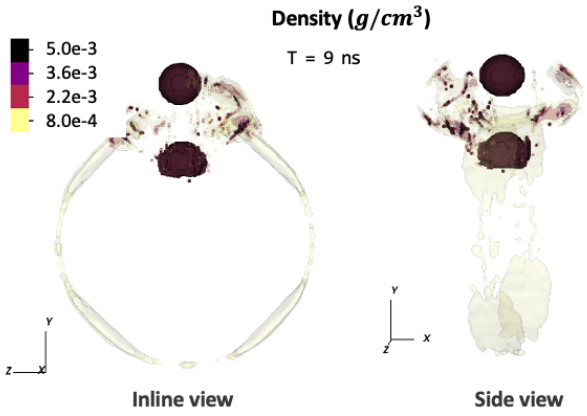

Fig. 7. Three dimensional PISALE simulation of three hydrogen droplets. The droplet following the XFEL heated droplet shields the second following droplet. The inline view is along the XFEL beam.

Surface tension can impact droplet dynamics in the lower temperature regions of this experiment. Early simulations show that enabling the surface tension package impacts the large-scale dynamics of the system. Figure 8 shows the side views of 3D PISALE simulations of hydrogen droplets with and without including surface tension effects. Even with surface tension forces included, the following droplet is still significantly perturbed by the exploding droplet. There is experimental evidence of larger water droplets heated by XFEL beams perturbing following droplets [24] but to our knowledge no published results for hydrogen droplets. Our modeling results for hydrogen show that fratricide is also a concern for these droplets and reduces the effective repetition rate.

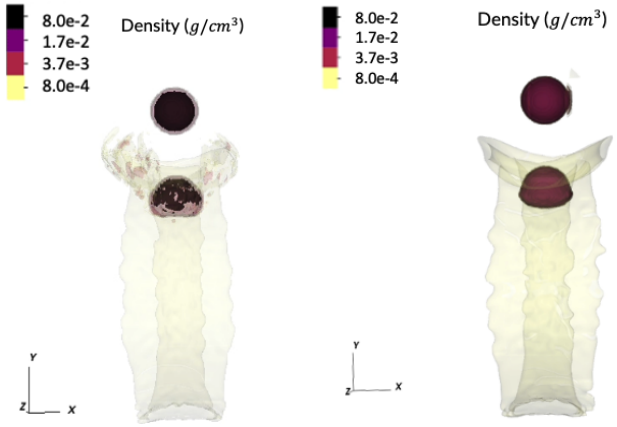

Fig. 8. Effects of surface tension are important for modeling. Comparison of PISALE simulation of hydrogen droplet heated by an XFEL without surface tension model (left) and including surface tension (right) at t = 8 ns.

IV. Conclusions and Future Work

The PISALE code is being used in a wide variety of new areas showing excellent agreement with experimental data and contributing to a basic understanding of the physical processes. Three dimensional simulations are critical to most of these physical processes, and this is enabled through modern HPC platforms and appropriate numerical techniques and programming models. The combination of AMR with ALE is a powerful numerical approach with unique capabilities. Significant physics effects can be included in the numerical methods with careful implementation of the operator splitting approach. We are exploring paths discretize a wider array of PDEs relevant to plasma physics, mesoscale material modeling, seismicity in geophysics, and electromagnetics. We are also exploring a FEM framework with 3D AMR capability that would improve the existing heat conduction, radiation diffusion, and surface tension models in PISALE.

Acknowledgment

We would like to thank additional members of the PISALE team for their expertise and contribution to the code. The PISALE code is supported by the National Science Foundation, under Office of Advanced Cyber Infrastructure Award Number 2005259, the U.S. Department of Energy, Office of Science, under Fusion Energy Sciences Research Division Award Numbers DE-SC0021374 and DE-SC0023475, and the Office of Naval Research (ONR), under ONR MURI Award Number N00014- 20-1-2682. This research used resources of the National Energy Research Scientific Computing Center (NERSC), a U.S. Department of Energy Office of Science User Facility located at Lawrence Berkeley National Laboratory, operated under Contract No. DE-AC02-05CH11231 using NERSC awards ERCAP0024761 and EERCAP0024762. The technical support and advanced computing resources from University of Hawaii Information Technology Services – Cyberinfrastructure, funded in part by the National Science

Copyright (c) IARIA, 2023. ISBN: 978-1-68558-107-7

Foundation MRI award Number 1920304, are gratefully acknowledged.

REFERENCES

[1] R. W. Anderson, N. S. Elliott, and R. B. Pember. "An arbitrary Lagrangian-Eulerian method with adaptive mesh refinement for the solution of the Euler equations". In: Journal of Computational Physics 199.2 (Sept. 2004), pp. 598–617.

[2] J. Barnard et al. "NDCX-II target experiments and simulations". In: Nuclear Instruments and Methods in Physics Research Section A: Accelerators, Spectrometers, Detectors and Associated Equipment 733 (2014), pp. 45–50.

[3] G. Bornia, A. Cervone, S. Manservisi, R. Scardovelli, and S. Zaleski. "On the properties and limitations of the height function method in two-dimensional Cartesian geometry". In: Journal of Computational Physics 230.4 (2011), pp. 851–862.

[4] J. U. Brackbill, D. B. Kothe, and C. Zemach. "A continuum method for modeling surface tension". In: J. Comput. Phys. 100 (1992), pp. 335–354.

[5] H.-J. G. Diersch. FEFLOW: finite element modeling of flow, mass and heat transport in porous and fractured media. Springer Science & Business Media, 2013.

[6] D. C. Eder, A. C. Fisher, A. E. Koniges, and N. D. Masters. "Modelling debris and shrapnel generation in inertial confinement fusion experiments". In: Nucl. Fusion 53 (2013), p. 113037.

[7] A. C. Fisher et al. "Modeling heat conduction and radiation transport with the diffusion Equation in NIF ALE-AMR". In: Journal of Physics: Conference Series 244 (2010), p. 022075.

[8] B. T. N. Gunney and R. W. Anderson. "Advances in patch-based adaptive mesh refinement scalability". In: Journal of Parallel and Distributed Computing 89 (2016), pp. 65–84.

[9] J. B. Habeck, M. D. Kroells, T. E. Schwartzentruber, and G. V. Candler. "Characterization of particle-surface impacts on a sphere-cone at hypersonic flight conditions". In: AIAA SCITECH 2023 Forum AIAA 2023-0205 (2023).

[10] A. Koniges et al. "Multi-material ALE with AMR for modeling hot plasmas and cold fragmenting materials". In: Plasma Sci. and Technol. 17 (2015), pp. 117–128.

[11] W. Liu et al. "Using a Korteweg-type model for modeling surface tension and its application". In: 54th Annual Meeting of the APS Division of Plasma Physics abstract id. BP8.058 (2012).

[12] W. Liu et al. "Surface tension models for a multi-material ALE code with AMR". In: Computers and Fluids 151 (2017), pp. 91–101.

[13] T. Ma et al. "Accelerating the rate of discovery: Toward high-repetition-rate HED science". In: Plasma Physics and Controlled Fusion 63.10 (2021), p. 104003.

[14] N. D. Masters, T. B. Kaiser, R. W. Anderson, D. C. Eder, A. C. Fisher, and A. E. Koniges. "Laser ray tracing in a parallel arbitrary Lagrangian-Eulerian adaptive mesh refinement hydrocode". In: Journal of Physics: Conference Series 244 (2010), p. 032022.

[15] J. McKee, Y. Mileyko, A. Fisher, and A. Koniges. "Developing a modern CFD framework with parallel algorithms and mesh adaption". In: Eleventh International Conference on Computational Fluid Dynamics (ICCFD11) (2022). Paper 1301.

[16] MFEM. https://mfem.org/. Accessed: 2023-09-18.

[17] MOOSE. https://mooseframework.inl.gov/. Accessed: 2023-09-18.

[18] C. Parisuana, D. C. Eder, M. Gauthier, C. Schoenwaelder, C. A. Stan, and S. H. Glenzer. "CFD modeling of droplets heated by an x-ray free electron laser". In: Eleventh International Conference on Computational Fluid Dynamics (ICCFD11) (2022). Paper 2003.

[19] T. Paula, S. Adami, and N. A. Adams. "Analysis of the early stages of liquid-water-drop explosion by numerical simulation". In: Physical Review Fluids 4.4 (2019), p. 044003.

[20] E. Pierazzo et al. "Validation of numerical codes for impact and explosion cratering: Impacts on strengthless and metal targets". In: Meteoritics & Planetary Science 43.12 (2008), pp. 1917–1938.

[21] I. Prencipe et al. "Targets for high repetition rate laser facilities: needs, challenges and perspectives". In: High Power Laser Science and Engineering 5 (2017), e17.

[22] M. A. Purvis et al. "Advancements in predictive plasma formation modeling". In: Proc. SPIE 9776. Extreme Ultraviolet (EUV) Lithography VII. 2016, 97760K–97760K.

[23] Y. Seo, J. Lee, A. Koniges, and A. Fisher. "Development of the PISALE codebase for simulating flow and transport in large-scale coastal aquifer". In: Eleventh International Conference on Computational Fluid Dynamics (ICCFD11) (2022). Paper 1502.

[24] C. A. Stan et al. "Liquid explosions induced by X-ray laser pulses". In: Nature Physics 12.10 (2016), pp. 966–971.

[25] C. A. Stan et al. "Negative pressures and spallation in water drops subjected to nanosecond shock waves". In: The journal of physical chemistry letters 7.11 (2016), pp. 2055–2062.

[26] M. L. Wilkins. Computer simulation of dynamic phenomena. Springer Science & Business Media, 1999.

[27] P. T. Yip et al. "Arbitrary Lagrangian Eulerian simulations of high speed particle impacts encountered during hypersonic flight". In: Eleventh International Conference on Computational Fluid Dynamics (ICCFD11) (2022). Paper 2202.

Copyright (c) IARIA, 2023. ISBN: 978-1-68558-107-7